46th AIAA/ASME/SAE/ASEE Joint Propulsion Conference & Exhibit
25 - 28 July 2010, Nashville, TN

AIAA 2010-6763

On the Viscous Bidirectional Vortex. Part 1: Linear Beltramian Motion

Joshua W. Batterson* and Joseph Majdalani†
University of Tennessee Space Institute, Tullahoma, TN 37388, USA

In this article, a viscous approximation is obtained for the linear, inviscid, Beltramian motion that may be engendered in a confined, bidirectional vortex chamber. Using the theory of matched-asymptotic expansions, viscous corrections are developed near the core region, where a forced vortex prevails, and near the cylindrical wall, where the no-slip requirement holds. Through proper scaling and variable transformations, a uniformly valid composite solution is subsequently constructed from which Majdalani's helical profile may be recovered in the inviscid limit. The latter was derived directly from first principles (see Majdalani, J., "Exact Eulerian Solutions of the Cylindrical Bidirectional Vortex," AIAA Paper 2009-5307, Denver, Colorado, Aug. 2009). However, because of its exact Eulerian nature, the strictly inviscid profile could not account for the effects of viscous stresses near the axis of rotation. The present approximation overcomes this deficiency by ensuring both the velocity adherence condition at the wall and the solid-body rotation of the forced vortex region. Being driven in large part by the inviscid character, the viscous-rectified swirl velocity component is also seen to exhibit small variations in the axial direction while continuing to vanish, as it should, at the sidewall. The advent of a viscous approximation enables us to quantify the size of the core and wall boundary layers, improve our prediction of the vorticity and pressure distributions, and relate most relevant flow features to the vortex Reynolds number.

Nomenclature

A_i	=	inlet area
B	=	tangential angular momentum, ru_θ
H	=	total stagnation pressure head, $p + \frac{1}{2}u^2$
Q_i	=	nondimensional volumetric flow rate, $\bar{Q}_i/(Ua^2)$
Re	=	injection Reynolds number, $Ua/\nu = 1/\varepsilon$
S	=	swirl number, $\pi ab/A_i = \pi\beta\sigma$
U	=	average inflow velocity in the tangential direction, $\bar{u}_\theta(a, L)$
V	=	vortex Reynolds number, $Q_i Re(a/L) = (\varepsilon\sigma l)^{-1} = 2\pi\kappa/\varepsilon$
$\bar{Q}_i$	=	inlet volumetric flow rate
$\boldsymbol{u}$	=	nondimensional velocity, $(\bar{u}_r, \bar{u}_\theta, \bar{u}_z)/U$
a	=	chamber radius
b	=	chamber outlet radius
l	=	chamber aspect ratio, L/a
p	=	nondimensional pressure, $\bar{p}/(\rho U^2)$
r, z	=	nondimensional radial and axial coordinates, $(\bar{r}, \bar{z})/a$
s	=	scaled radial coordinate

Subscripts

0	=	reference value at the chamber headwall
θ	=	tangential component
c	=	represents a solution in the core
i	=	inlet property
m	=	mode number
r, z	=	radial or axial component
w	=	represents a solution near the wall

*Graduate Research Assistant, Mechanical, Aerospace and Biomedical Engineering Department. Student Member AIAA.
†H. H. Arnold Chair of Excellence in Advanced Propulsion, Mechanical, Aerospace and Biomedical Engineering Department. Senior Member AIAA. Fellow ASME.

Symbols

α = constant, $\frac{\lambda_0}{2\beta J_1(\lambda_0\beta)}\left(\frac{1}{8}\lambda_0^2 - 1\right)$
β = normalized outlet radius, b/a
δ = characteristic boundary layer thickness
δ_p = location of maximum pressure gradient
ε = viscous parameter, $1/Re = \nu/(Ua)$
γ = constant, $\frac{\lambda_0}{4\beta J_1(\lambda_0\beta)}$
κ = inflow parameter, $Q_i/(2\pi l) = (2\pi\sigma l)^{-1}$
λ = eigenvalue
ν = kinematic viscosity
ω_f = constant angular speed of the forced vortex
$\boldsymbol{\omega}$ = vorticity vector
ψ = streamfunction
ρ = density
σ = modified swirl number, $Q_i^{-1} = S/(\pi\beta)$
υ = separation constant

Superscripts

$\bar{}$ = overbars denote a dimensional variable
c = denotes a composite solution
ci = denotes a composite-inner solution
i = denotes an inner solution
o = denotes an outer solution
w = denotes a near-wall solution

I. Introduction

Characterization of helical flows continues to occupy a central role in fluid dynamics due to its relevance to several phenomenological applications. Aside from its role in engineering research, fundamental understanding of swirl-dominated motions has proved to be quintessential to a number of widely dissimilar fields ranging from meteorology, oceanography, astronomy and astrophysics, to astrology and mythology.[1–3] For example, the identification and discussion of a tidal whirlpool *Charybdis* may be traced back to Book XII of the Odyssey where fascination in naturally occurring cyclonic motions could already be seen, especially amongst ancient navigators.[4]

Returning to the present epoch, a simple solution by Rankine[5] may be cited as one that has evolved from a piecewise-defined, non-differentiable, basic approximation to a useful one-dimensional, external, swirling flow model, to an integral part of multi-directional internal flows.[6] In fact, Rankine's approximation continues to receive attention today in the works of Kurosaka,[7] Wu,[8] Ashill *et al.*[9] and Di Cicca *et al.*[10] Other notable advances may be attributed to Lamb[11] and Oseen[12] whose classical model incorporates the temporal decay of an external vortex. In similar context, Burgers[13,14] and Rott[15,16] have introduced a vortex profile that resembles that of Lamb and Oseen, with the difference being in its weak spatial dependence versus Lamb-Oseen's time dependence. In fact, as shown by Batterson, Maicke and Majdalani,[17] both Lamb-Oseen and Burgers-Rott profiles may be normalized by their characteristic dimensions and expressed by a single, equivalent Gaussian vortex function.[18]

Unlike the aforementioned formulations that mainly pertain to unidirectional vortices, much fewer profiles may be found in which bidirectionality is permitted. The earliest bidirectional motion could perhaps be connected with Sullivan's *two-cell* vortex.[19] Due to its distinct inner down-flow often seen in tornados, Sullivan's model was shown to possess considerable relevance in meteorological studies.[8] As for industrial applications, Bloor and Ingham[20] may have been the first to develop a self-contained theoretical model in the context of cyclone separators. In their 1987 work, they manage to introduce an inviscid approximation to a conical vortex chamber that mimics the bulk motion in flow separators. Their solution is later reconstructed and extended by Barber and Majdalani.[21] Though profound in its application, their solution displayed a centerline singularity while allowing slip at the sidewall.

In the propulsion community, the utilization of bidirectional motion was first proposed by Gloyer, Knuth and Goodman[22] as a means to enhance the burn-rate in hybrid rocket engines. It was further developed by Knuth *et al.*,[23] Chiaverini *et al.*,[24] and other workers who helped to mature the technology of the so-called Vortex Injection Hybrid

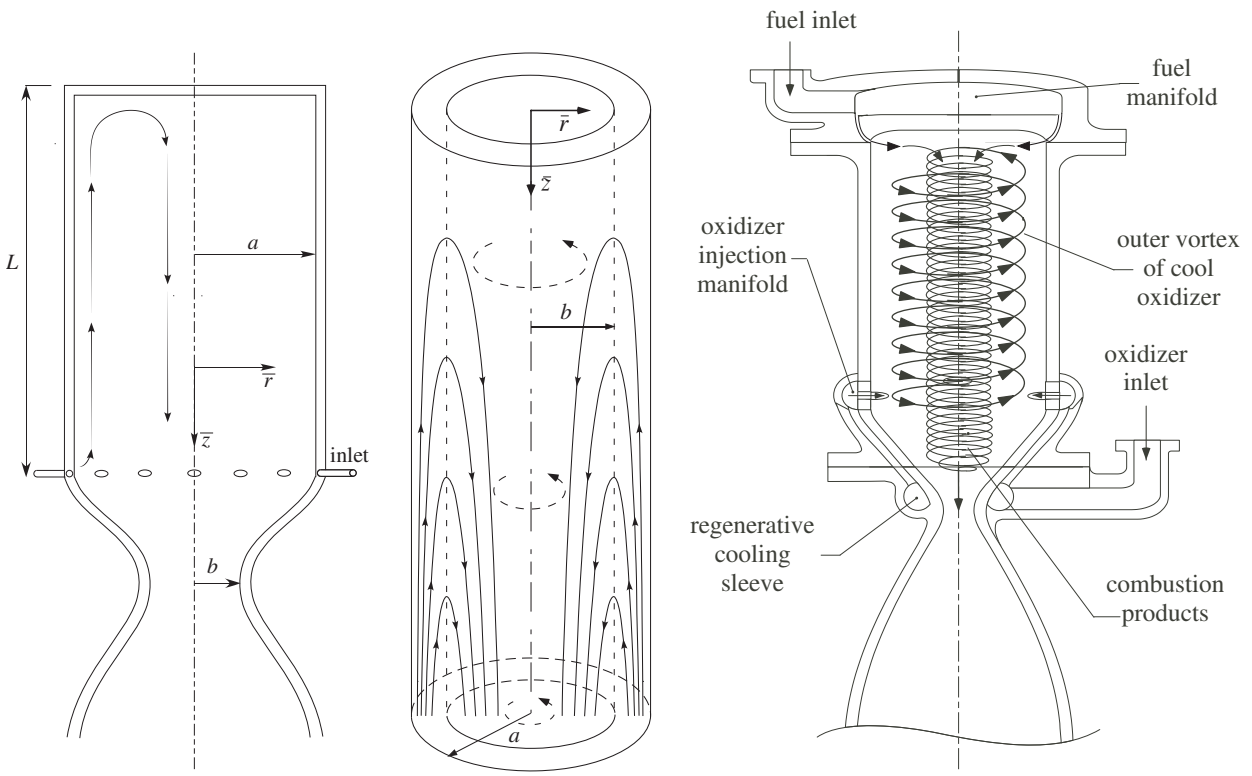

a) Geometry and coordinate system **b)** Flowfield characteristics **c)** VCCWC schematic

Figure 1. Geometry and schematic of the bidirectional vortex chamber showing a) the coordinate system, b) the essential flow characteristics, and c) the VCCWC prototype.

Rocket Engine (VIHRE) and the Vortex Combustion Cold-Wall Chamber (VCCWC) shown schematically in Fig. 1. The latter refers to an internally cooled liquid thrust chamber driven by a pair of coaxial vortices. Today, the topic of vortex-fired engines is featured as an integral theme in the propulsion industry. Naturally, the inception of the VCCWC provided the impetus for Vyas and Majdalani[25] and Majdalani and Rienstra[26] to derive the first three-component, complex-lamellar, inviscid model that describes the observed cyclonic behavior. Deficiencies in their purely inviscid profile were analogous to those encountered by Bloor and Ingham.[20] Uniformly valid viscous approximations were therefore needed and these were presented by Majdalani and Chiaverini[27] who overcame the centerline singularity while securing the velocity adherence condition at the sidewall. Shortly thereafter, Batterson and Majdalani[28] managed to incorporate viscous wall corrections in the remaining axial and radial directions, thus arriving at a fully regularized velocity field.

Following the complete characterization of the complex-lamellar model, Majdalani[29] utilized the incompressible Bragg-Hawthorne equation to produce additional helical solutions that describe the bidirectional motion in right-cylindrical chambers. Two of the new profiles were of the Beltramian type and displayed either linear or nonlinear spatial dependence. They were characterized by a zero Lamb vector, $\bar{\boldsymbol{\omega}} \times \bar{\boldsymbol{u}} = 0$, to the extent that their vorticity and velocity remained directly proportional through $\bar{\boldsymbol{\omega}} = \lambda_0 \bar{\boldsymbol{u}}$.[30] As one would expect, these models also shared their predecessor's inviscid nature and limitations in regions where fluid friction could not be ignored.

In this three-part paper series, the inviscid Beltramian models will be enhanced through the addition of viscous corrections. These will be shown to overcome their blatant singularities at the centerline and prevent slip from occurring at the sidewall in all three spatial directions, axial, radial, and tangential. To this end, the present article will be devoted to the treatment of the linear model; the analysis of the nonlinear counterpart will be deferred to the companion paper labeled Part 2. In Part 3, the solutions corresponding to multi-directional flow reversals will be examined. In the process, a systematic spatial reduction of the governing equations will be undertaken with the aim of simplifying the Navier-Stokes equations and retrieving a set of relevant boundary layer equations.[28,31] These asymptotic maneuvers will render the original nonlinear equations linear and solvable. The corresponding viscous

corrections will be extracted and matched to the outer, inviscid model, thus resulting in a uniformly valid, composite approximation for each vector component.

II. Formulation

The formulation of the inviscid problem follows precisely the steps delineated by Majdalani.[29] In the interest of clarity, these are repeated below.

A. Governing Equations

Using standard nomenclature and the geometry shown in Fig. 1b, we define

$$\begin{cases} z = \dfrac{\bar{z}}{a}; \quad r = \dfrac{\bar{r}}{a}; \quad \nabla = a\bar{\nabla}; \quad u_r = \dfrac{\bar{u}_r}{U}; \quad u_\theta = \dfrac{\bar{u}_\theta}{U}; \quad u_z = \dfrac{\bar{u}_z}{U} \\ p = \dfrac{\bar{p}}{\rho U^2}; \quad H = \dfrac{\bar{H}}{\rho U^2}; \quad B = \dfrac{\bar{B}}{aU}; \quad Q_i = \dfrac{\bar{Q}_i}{Ua^2} = \sigma^{-1}; \quad l = \dfrac{L}{a} \end{cases} \tag{1}$$

According to this nondimensionalization scheme, Euler's equation may be compacted into

$$\nabla H - \boldsymbol{u} \times \boldsymbol{\omega} = 0; \quad H = \tfrac{1}{2}\boldsymbol{u} \cdot \boldsymbol{u} + p \tag{2}$$

where H denotes the total fluid head. As usual, the Stokes streamfunction can be written as

$$u_r = -\frac{1}{r}\frac{\partial \psi}{\partial z}; \quad u_z = \frac{1}{r}\frac{\partial \psi}{\partial r} \tag{3}$$

Equation (2) may also be expanded into component form. The result is

continuity:

$$\frac{1}{r}\frac{\partial (ru_r)}{\partial r} + \frac{\partial u_z}{\partial z} = 0 \tag{4}$$

r-momentum:

$$u_r\frac{\partial u_r}{\partial r} + u_z\frac{\partial u_r}{\partial z} - \frac{u_\theta^2}{r} = -\frac{\partial p}{\partial r} \tag{5}$$

θ-momentum:

$$u_r\frac{\partial u_\theta}{\partial r} + \frac{u_\theta u_r}{r} = 0 \quad \text{or} \quad \frac{1}{r}\frac{\partial (ru_\theta)}{\partial r} = 0 \tag{6}$$

z-momentum:

$$u_r\frac{\partial u_z}{\partial r} + u_z\frac{\partial u_z}{\partial z} = -\frac{\partial p}{\partial z} \tag{7}$$

The vorticity in this case reduces to

$$\boldsymbol{\omega} = -\frac{\partial u_\theta}{\partial z}\boldsymbol{e}_r + \left(\frac{\partial u_r}{\partial z} - \frac{\partial u_z}{\partial r}\right)\boldsymbol{e}_\theta + \frac{1}{r}\frac{\partial (ru_\theta)}{\partial r}\boldsymbol{e}_z \tag{8}$$

B. The Bragg-Hawthorne Equation

At this juncture, the θ-momentum equation may be readily integrated to obtain

$$ru_\theta = B(\psi) \tag{9}$$

where $B(\psi)$ represents the tangential angular momentum. It may be related to the radial vorticity by substituting u_θ into the first member of Eq. (8). This gives

$$\omega_r = -\frac{\partial u_\theta}{\partial z} = -\frac{1}{r}\frac{\partial (ru_\theta)}{\partial z} = -\frac{1}{r}\frac{\partial B}{\partial z} = -\frac{1}{r}\frac{\mathrm{d}B}{\mathrm{d}\psi}\frac{\partial \psi}{\partial z} \tag{10}$$

Along similar lines, the tangential vorticity may be retrieved from the axial component of Eq. (2), namely,

$$\frac{\partial H}{\partial z} + u_\theta \omega_r - u_r \omega_\theta = \frac{\mathrm{d}H}{\mathrm{d}\psi}\frac{\partial \psi}{\partial z} + u_\theta \omega_r - u_r \omega_\theta \tag{11}$$

By substituting Eqs. (3), (9), and (10) into Eq. (11), ω_θ may be readily extracted. This operation yields

$$\frac{\mathrm{d}H}{\mathrm{d}\psi}\frac{\partial \psi}{\partial z} - \frac{B}{r^2}\frac{\mathrm{d}B}{\mathrm{d}\psi}\frac{\partial \psi}{\partial z} + \frac{1}{r}\frac{\partial \psi}{\partial z}\omega_\theta = 0 \quad \text{or} \quad \frac{\omega_\theta}{r} = -\frac{\mathrm{d}H}{\mathrm{d}\psi} + \frac{B}{r^2}\frac{\mathrm{d}B}{\mathrm{d}\psi} \tag{12}$$

Finally, Eq. (12) may be equated to its counterpart in Eq. (8) to arrive at

$$\frac{\partial^2 \psi}{\partial r^2} - \frac{1}{r}\frac{\partial \psi}{\partial r} + \frac{\partial^2 \psi}{\partial z^2} = r^2 \frac{\mathrm{d}H}{\mathrm{d}\psi} - B\frac{\mathrm{d}B}{\mathrm{d}\psi} \tag{13}$$

We hence recover the celebrated Bragg-Hawthorne equation in cylindrical coordinates.[32]

C. Three Families of Solutions

Once the streamfunction is realized, so will the radial and axial velocities. As for the swirl velocity, it is closely intertwined with the tangential angular momentum, B. The latter must be specified according to the conditions associated with the physical problem. While many possibilities exist for the choice of B, most do not lead to analytically tractable solutions unless the right-hand-side of Eq. (13) is constant or linear in ψ. Two previously considered cases are

$$\begin{cases} B\dfrac{\mathrm{d}B}{\mathrm{d}\psi} = 0; & B = B_0 = 1 & \text{Vyas and Majdalani}[25] \\ B\dfrac{\mathrm{d}B}{\mathrm{d}\psi} = \text{const}; & B = \sqrt{B_0\psi + B_1} & \text{Bloor and Ingham}[20] \end{cases} \tag{14}$$

Here we allow this term to be a linear function of ψ such that

$$B\frac{\mathrm{d}B}{\mathrm{d}\psi} = f(\psi) = C_m^2 \psi; \quad B = \sqrt{C_m^2 \psi^2 + B_1} \tag{15}$$

Without loss of generality, the constant C_m^2 is specified in this particular fashion to facilitate later manipulations. Moreover, the Bragg-Hawthorne equation may be substantially simplified when taking into account the invariance of the total enthalpy along individual streamlines. Thus by putting

$$\frac{\mathrm{d}H}{\mathrm{d}\psi} = 0 \tag{16}$$

on the right-hand-side of Eq. (13), we are left with

$$\frac{\partial^2 \psi}{\partial r^2} - \frac{1}{r}\frac{\partial \psi}{\partial r} + \frac{\partial^2 \psi}{\partial z^2} + C_m^2 \psi = 0 \tag{17}$$

This equation is a linear, separable PDE. Its solution may be determined using the functional decomposition $\psi = f(r)g(z)$. As shown by Majdalani,[29] we find

$$-\frac{\ddot{g}}{g} = \frac{1}{f}\left(f'' - \frac{1}{r}f' + C_m^2 f\right) = \begin{cases} 0 \\ +\upsilon^2 \\ -\upsilon^2 \end{cases} \tag{18}$$

The right-hand-side delineates three possible separation constants. The first leads to a linear axial dependence and will be addressed below. The second choice leads to a harmonic axial dependence that will be discussed in the second installment of this work. The third returns solutions that appear to be unphysical when taken separately.

D. The Linear Beltramian Solution

Using $\upsilon = 0$, the linear axial dependence emerges from $g(z)$, viz.

$$g(r) = C_1 z + C_2 \tag{19}$$

The radial expression returns a simple Bessel equation that yields

$$f(r) = r\left[C_3 J_1(C_m r) + C_4 Y_1(C_m r)\right] \tag{20}$$

The general solution of Eq. (17) may be synthesized from the product of $f(r)$ and $g(z)$. One gets

$$\psi = r(C_1 z + C_2)\left[C_3 J_1(C_m r) + C_4 Y_1(C_m r)\right] \tag{21}$$

As for the boundary conditions, we retrace those employed by Majdalani[29] and set

$$z = 0; \quad u_z(r,0) = 0 \quad \text{or} \quad \frac{1}{r}\frac{\partial \psi(r,0)}{\partial r} = 0 \tag{22a}$$

$$r = 0; \quad u_r(0,z) = 0 \quad \text{or} \quad -\frac{1}{r}\frac{\partial \psi(0,z)}{\partial z} = 0 \tag{22b}$$

$$r = 1; \quad u_r(1,z) = 0 \quad \text{or} \quad -\frac{1}{r}\frac{\partial \psi(1,z)}{\partial z} = 0 \tag{22c}$$

$$z = l; \quad Q_i = \int_0^{\beta}\int_0^{2\pi} \boldsymbol{u}\cdot\boldsymbol{n}\, r\,\mathrm{d}r = 2\pi\int_0^{\beta} u_z(r,l) r\,\mathrm{d}r = 2\pi\int_0^{\beta}\frac{1}{r}\frac{\partial \psi(r,l)}{\partial r}\, r\,\mathrm{d}r \tag{22d}$$

Equation (22a) represents a hardwall boundary condition that prevents crossflow at the headwall. From this condition two constants may be retrieved. For boundedness we must have $C_4 = 0$, and for zero axial injection at the headwall, we reap $C_2 = 0$. The remaining expression becomes

$$\psi = \psi_0 z r J_1(C_m r); \quad \psi_0 = C_3 C_1 \tag{23}$$

Ordinarily, Eq. (22b) may be used to enforce axisymmetry by disallowing crossflow along the centerline. However, we find this condition to be self-satisfying and, hence, inconsequential.

At this point, Eq. (22c) may be used to disallow crossflow along the sidewalls. This condition gives rise to an eigenvalue equation of the form $J_1(C_m) = 0$. Its eigenvalues correspond to the roots of the Bessel function of the first kind, $C_m = \lambda_m$, where $\lambda_m = \{3.83171, 7.01559, 10.1735, 13.3237, ...\}$. Given that this work is only concerned with simple bidirectional motions, only the case of $\lambda_m = \lambda_0 = 3.83171$ will be considered. Higher eigenvalues taken separately lead to multiple flow reversals that are discussed in the third installment of this work.

Lastly, Eq. (22d) may be used to enforce mass conservation by requiring the injected flow to evacuate the chamber through the exit port. This fixes the last constant at $\psi_0 = Q_i/[2\pi l \beta J_1(\lambda_0 \beta)]$. We therefore collect,

$$\psi = \kappa z r \frac{J_1(\lambda_0 r)}{\beta J_1(\lambda_0 \beta)} \tag{24}$$

where $\kappa = Q_i/(2\pi l)$.

With the streamfunction at hand, Eq. (3) may be used to deduce the axial and radial velocities. Along similar lines, Eq. (15) may be used to determine u_θ within a constant, specifically one that can be obtained from the use of $u_\theta(1,l) = 1$. This last condition ensures that u_θ matches the tangential velocity in the injection plane. The complete inviscid velocity profile becomes

$$\boldsymbol{u} = -\kappa\frac{J_1(\lambda_0 r)}{\beta J_1(\lambda_0\beta)}\boldsymbol{e}_r + r^{-1}\sqrt{1 + \frac{\lambda_0^2\kappa^2 r^2 z^2 J_1^2(\lambda_0 r)}{\beta^2 J_1^2(\lambda_0\beta)}}\boldsymbol{e}_\theta + \lambda_0\kappa z\frac{J_0(\lambda_0 r)}{\beta J_1(\lambda_0\beta)}\boldsymbol{e}_z \tag{25}$$

III. Viscous Corrections

Recent work by Majdalani and Chiaverini[27] and, later, by Batterson and Majdalani[28] describe an *approximate* strategy that can be used to obtain boundary layer corrections to a complex-lamellar swirl-dominated profile. The same procedure can be applied to the linear Beltramian model with the aim of characterizing its axial, radial, and tangential boundary layers. As shown in these previous studies, the boundary layer equations may be systematically identified by starting with the Navier-Stokes equations and dismissing terms that may be deemed of higher order in the viscous layer. Then through a series of asymptotic approximations, the boundary layer equations may be scaled and linearized, solved asymptotically, and matched to the outer inviscid solution defined by Eq. (25).

A. Tangential Wall and Core Corrections

By their very nature, inviscid representations such as those discussed above are, quite often, too limited to observe the zero velocity condition along slip planes. In the case of the tangential velocity, beyond its disparity near the sidewall, it diverges near the core. In this region, viscous forces dominate and lead to the establishment of a forced vortex. The forced vortex exhibits solid body rotation and suppresses the unbounded behavior plaguing the inviscid model.

In order to properly capture the viscous core effects, one applies an order of magnitude reduction of the tangential momentum equation. This is accomplished by assuming that velocities and coordinate directions parallel to the primary flow direction are of order unity, while those perpendicular are of $O(\delta)$. Following convention the dimensionless viscosity $\nu/(Ua)$ may be taken at $O(\delta^2)$.[31] Finally, terms of $O(\delta)$ and above may be truncated, thus leaving us with

$$\frac{u_r}{r}\frac{\partial}{\partial r}(ru_\theta) + u_z\frac{\partial u_\theta}{\partial z} = \varepsilon\left\{\frac{\partial}{\partial r}\left[\frac{1}{r}\frac{\partial}{\partial r}(ru_\theta)\right]\right\}; \quad \varepsilon = \frac{\nu}{Ua} = Re^{-1} \tag{26}$$

Through careful observation of the inviscid formulation, it may be seen that axial variations are only realized in the outer region away from the viscous core or sidewall. Near the core, the inviscid solution smoothly approaches the axially invariant function $1/r$. Near the sidewall, the inviscid profile smoothly converges to a value of unity at any axial position. This behavior warrants a further reduction in Eq. (26). In fact, the elimination of derivatives with respect to z was equally undertaken by Majdalani and Chiaverini.[27] Along similar lines, the ensuing ODE may be subjected to the dependent-variable transformation, $u_\theta = \xi_\theta(r)/r$, whence it can be written as

$$\varepsilon\left(\frac{\mathrm{d}^2\xi_\theta}{\mathrm{d}r^2} - \frac{1}{r}\frac{\mathrm{d}\xi_\theta}{\mathrm{d}r}\right) - u_r\frac{\mathrm{d}\xi_\theta}{\mathrm{d}r} = 0 \tag{27}$$

At this point, the inviscid solution, wherein the condition $u_r = 0$ is self-satisfied at the sidewall, may be taken as an accurate leading-order approximation to the radial velocity inside the boundary layer. This assumption is corroborated by previous studies[27,28] where viscosity was shown to have little bearing on the radial velocity profile near the boundary layer. The problem simplifies substantially when considering the coefficient, u_r, to be inviscid. The updated equation becomes

$$\varepsilon\left(\frac{\mathrm{d}^2\xi_\theta}{\mathrm{d}r^2} - \frac{1}{r}\frac{\mathrm{d}\xi_\theta}{\mathrm{d}r}\right) + \kappa\frac{J_1(\lambda_0 r)}{\beta J_1(\lambda_0\beta)}\frac{\mathrm{d}\xi_\theta}{\mathrm{d}r} = 0 \tag{28}$$

1. Forced Core Vortex

Equation (28) is a valid starting point for studying either the viscous core or sidewall boundary layers. In order to rescale the core region, a stretched coordinate transformation may be employed. We take $s = r/\delta$, where δ denotes the characteristic boundary layer thickness. Substituting this transformation and its derivatives into Eq. (28) returns the boundary layer equation properly expressed in the core region. We get

$$\varepsilon\left(\frac{\mathrm{d}^2\xi_\theta^{(i)}}{\mathrm{d}s^2} - \frac{1}{s}\frac{\mathrm{d}\xi_\theta^{(i)}}{\mathrm{d}s}\right) + \kappa\delta\frac{J_1(\lambda_0\delta s)}{\beta J_1(\lambda_0\beta)}\frac{\mathrm{d}\xi_\theta^{(i)}}{\mathrm{d}s} = 0 \tag{29}$$

where the superscript 'i' refers to an 'inner' solution. Its associated boundary conditions are

$$\begin{cases} \xi_\theta^{(i)}(0) = 0 \\ \lim\limits_{s\to\infty}\xi_\theta^{(i)} = \lim\limits_{r\to 0}\xi_\theta^{(o)} = 1 \end{cases} \tag{30}$$

where $\xi_\theta^{(o)} = ru_\theta^{(o)}$. Note that the conditions in Eq. (30) act, at the left end of the interval, to remove the singularity at the centerline and, at the right end, to asymptotically approach the inviscid profile in the outer domain in accordance with Prandtl's matching principle.[33]

In order for the diffusive and convective terms to balance, the parameters controlling their respective magnitudes must be of the same order. In our case, the three small parameters ε, δ, and κ must be carefully ordered. To do so, we first expand the coefficient of the convective term. By writing the Bessel function as $J_1(\lambda_0\delta s) \approx \lambda_0\delta s/2 + O(\delta^2)$, the convective term may be seen, based on Eq. (29), to be of $O(\kappa\delta^2)$. Then for the diffusive and convective terms to balance one must have $\delta \sim \sqrt{\varepsilon/\kappa}$. This so-called *distinguished limit* for δ may be substituted back into the representative equation to the extent of producing

$$\frac{\mathrm{d}^2\xi_\theta^{(i)}}{\mathrm{d}s^2} + \left[\frac{\lambda_0 s}{2\beta J_1(\lambda_0\beta)} - \frac{1}{s}\right]\frac{\mathrm{d}\xi_\theta^{(i)}}{\mathrm{d}s} = 0 \tag{31}$$

Fortuitously, by only retaining the leading-order expansion of the convective coefficient, we incur a maximum error on the order of 2-10% for realistic values of ε and κ. The solution for Eq. (31) becomes

$$\xi_\theta^{(i)} = -\frac{2C_1\beta J_1(\lambda_0\beta)}{\lambda_0}\exp\left[-\frac{\lambda_0 s^2}{4\beta J_1(\lambda_0\beta)}\right] + C_2 \tag{32}$$

Thus by applying the left-end boundary condition, we get

$$C_2 = \frac{2C_1\beta J_1(\lambda_0\beta)}{\lambda_0} \quad \text{or} \quad \xi_\theta^{(i)} = \frac{2C_1\beta J_1(\lambda_0\beta)}{\lambda_0}\left\{1 - \exp\left[-\frac{\lambda_0 s^2}{4\beta J_1(\lambda_0\beta)}\right]\right\} \tag{33}$$

The last constant C_1 may be retrieved from the right-end boundary condition, namely,

$$C_1 = \frac{\lambda_0}{2\beta J_1(\lambda_0\beta)} \quad \text{or} \quad \xi_\theta^{(i)} = 1 - \exp\left[-\frac{\lambda_0 s^2}{4\beta J_1(\lambda_0\beta)}\right] \tag{34}$$

At this juncture, a uniformly valid composite solution may be constructed using Erdélyi's technique for the treatment of matched-asymptotic expansions.[34] Accordingly, the inviscid outer solution may be mated with the inner viscous approximation to render a composite-inner solution

$$\xi_\theta^{(ci)} = \xi_\theta^{(o)} + \xi_\theta^{(i)} - \lim_{r\to 0}\xi_\theta^{(o)} \quad \text{or} \quad \xi_\theta^{(ci)} = \left[1 + \frac{\lambda_0^2\kappa^2 r^2 z^2 J_1^2(\lambda_0 r)}{\beta^2 J_1^2(\lambda_0\beta)}\right]^{1/2} - \exp\left[-\frac{\kappa\lambda_0 r^2}{4\varepsilon\beta J_1(\lambda_0\beta)}\right] \tag{35}$$

In terms of u_θ, the uniformly valid solution reads

$$u_\theta^{(ci)} = \frac{1}{r}\left\{\left[1 + \frac{\lambda_0^2\kappa^2 r^2 z^2 J_1^2(\lambda_0 r)}{\beta^2 J_1^2(\lambda_0\beta)}\right]^{1/2} - \exp\left[-\frac{\lambda_0 V r^2}{8\pi\beta J_1(\lambda_0\beta)}\right]\right\}; \quad V = \frac{2\pi\kappa}{\varepsilon} \tag{36}$$

The similarity parameter V is referred to as the *vortex Reynolds number*. It was first identified by Majdalani in the treatment of the complex-lamellar flow analog.[27,35] Its utilization in laminar and turbulent flows was further discussed by Maicke and Majdalani.[36] Therein, an over-prediction of the maximum velocities was shown to occur under turbulent conditions unless an effective value of V was used, specifically one that was based on an increased turbulent eddy viscosity.

Based on Eq. (36) we are able to determine the constant angular speed, ω_f, of the forced vortex. By expanding $u_\theta^{(ci)}$ near $r = 0$, we find

$$u_\theta^{(ci)} \approx \frac{V\lambda_0}{8\pi\beta J_1(\lambda_0\beta)}r + \frac{\left(-V^2\lambda_0^2 + 16\pi^2 z^2\kappa^2\lambda_0^4\right)}{128\pi^2\beta^2 J_1^2(\lambda_0\beta)}r^3 + O(r^5) \tag{37}$$

This expression shows that a linear relationship $u_\theta^{(ci)} \approx \omega_f r$ emerges in the vicinity of the centerline with

$$\omega_f = \frac{V\lambda_0}{8\pi\beta J_1(\lambda_0\beta)} \approx 0.467919V \tag{38}$$

It is interesting that ω_f is nearly twice as large as its counterpart encountered in the complex-lamellar analysis wherein $\omega_f = 0.25V$.[27] This near doubling in speed seems to characterize several features common to these two models.

2. Sidewall Boundary Layer

In rescaling the viscous wall region, the independent-variable transformation $s = (1 - r)/\delta$ may be inserted into Eq. (28) such that

$$\varepsilon\left[\frac{\mathrm{d}^2\xi_\theta^{(w)}}{\mathrm{d}s^2} + \frac{\delta}{(1-s\delta)}\frac{\mathrm{d}\xi_\theta^{(w)}}{\mathrm{d}s}\right] - \kappa\delta\frac{J_1\left[\lambda_0\left(1-s\delta\right)\right]}{\beta J_1\left(\lambda_0\beta\right)}\frac{\mathrm{d}\xi_\theta^{(w)}}{\mathrm{d}s} = 0 \tag{39}$$

where 'w' refers to an inner wall approximation. As before a suitable series expansion may be developed for the convective term. For example, one may put

$$J_1\left(\lambda_0 x\right) \approx \frac{\lambda_0 x}{2} - \frac{\lambda_0^3 x^3}{16} \approx -\frac{\lambda_0}{2}\left(\frac{\lambda_0^2}{8} - 1\right) + O\left(\delta\right); \quad x = (1 - \delta s) \tag{40}$$

In this case, terms of $O(\delta)$ are ignored as retention of higher order terms may be shown to be immaterial. It may also be seen that the coefficient of the convective part appears at $O(\kappa\delta)$. The corresponding distinguished limit, $\delta \sim \varepsilon/\kappa$, may be substituted back along with expanded convective coefficient to obtain

$$\frac{\mathrm{d}^2\xi_\theta^{(w)}}{\mathrm{d}s^2} + \alpha\frac{\mathrm{d}\xi_\theta^{(w)}}{\mathrm{d}s} = 0; \qquad \alpha = \frac{\lambda_0}{2\beta J_1\left(\lambda_0\beta\right)}\left(\frac{\lambda_0^2}{8} - 1\right) \tag{41}$$

where curvature terms are discounted, being of higher order. A solution for Eq. (41) may be expressed as

$$\xi_\theta^{(w)} = C_2 - \frac{C_1}{\alpha}e^{-\alpha s} \tag{42}$$

At this point, a pair of boundary conditions may be used that mirror those used in the core region. These consist of the no-slip at the sidewall and asymptotic matching in the outer region:

$$\begin{cases} \xi_\theta^{(w)}\left(0\right) = 0 \\ \lim\limits_{s\to\infty}\xi_\theta^{(w)}\left(s\right) = \lim\limits_{r\to 1}\xi_\theta^{(o)}\left(r\right) = 1 \end{cases} \tag{43}$$

Because the core corrections have no influence at the sidewall, $\xi_\theta^{(o)}$ may be used rather than the inner composite solution specified by Eq. (35). Following the application of Eq. (43), the inner, near-wall solution may be determined to be

$$\xi_\theta^{(w)} = 1 - \exp\left[-\frac{\lambda_0}{2\beta J_1\left(\lambda_0\beta\right)}\left(\frac{\lambda_0^2}{8} - 1\right)s\right] \tag{44}$$

The total composite solution is thus at hand. In terms of original variables, we collect

$$\xi_\theta^{(c)} = \xi_\theta^{(ci)} + \xi_\theta^{(w)} - \lim_{s\to\infty}\xi_\theta^{(w)}\left(s\right) \tag{45}$$

or

$$u_\theta^{(c)} = \frac{1}{r}\left\{\left[1 + \frac{\lambda_0^2\kappa^2 r^2 z^2 J_1^2\left(\lambda_0 r\right)}{\beta^2 J_1^2\left(\lambda_0\beta\right)}\right]^{1/2} - \exp\left[-\frac{\lambda_0 V r^2}{8\pi\beta J_1\left(\lambda_0\beta\right)}\right] - \exp\left[-\frac{\lambda_0 V}{4\pi\beta J_1\left(\lambda_0\beta\right)}\left(\frac{\lambda_0^2}{8} - 1\right)(1 - r)\right]\right\} \tag{46}$$

This expression overcomes the issue of unboundedness at the core while fulfilling the physical requirement of no slip at the sidewall.

B. Axial Wall Correction

Unlike its tangential counterpart, the axial velocity is not marred by a centerline singularity. Its only deficiency materializes at the sidewall. Using a similar procedure to that outlined above, an order of magnitude reduction leads to a compact axial momentum equation of the form

$$u_r\frac{\partial u_z}{\partial r} + u_z\frac{\partial u_z}{\partial z} = -\frac{\partial p}{\partial z} + \varepsilon\left(\frac{\partial^2 u_z}{\partial r^2} + \frac{1}{r}\frac{\partial u_z}{\partial r}\right) \tag{47}$$

In the above, the remaining convective term may be linearized by replacing u_r with its inviscid, leading-order representation u_r^o. Then realizing that the axial invariance of the tangential boundary layer thickness requires spatial invariance in the axial direction,[28,37] Eq. (47) may be approximated by

$$\varepsilon\left(\frac{\partial^2 u_z}{\partial r^2}+\frac{1}{r}\frac{\partial u_z}{\partial r}\right)+\kappa\frac{J_1(\lambda_0 r)}{\beta J_1(\lambda_0\beta)}\frac{\partial u_z}{\partial r}=0 \tag{48}$$

Next, in order to suitably accommodate the spatially varying outer condition on u_z, a dependent-variable transformation is implemented. In comparison, the tangential velocity equation underwent a less intrusive transformation given the constancy of the angular momentum in the outer limit of Eq. (43). In the spirit of presenting a systematic transformation, we substitute $u_z=\xi_z(r)zJ_0(\lambda_0 r)$ into Eq. (48) and write

$$\begin{aligned}\varepsilon\Bigg\{zJ_0(\lambda_0 r)\xi_z''-\frac{z\lambda_0^2}{2}\left[J_0(\lambda_0 r)-J_2(\lambda_0 r)\right]\xi_z\\ -2z\lambda_0 J_1(\lambda_0 r)\xi_z'+\frac{1}{r}\left[-z\lambda_0 J_1(\lambda_0 r)\xi_z+zJ_0(\lambda_0 r)\xi_z'\right]\Bigg\}\\ +\kappa\frac{J_1(\lambda_0 r)}{\beta J_1(\lambda_0\beta)}\left[-z\lambda_0 J_1(\lambda_0 r)\xi_z+zJ_0(\lambda_0 r)\xi_z'\right]=0\end{aligned} \tag{49}$$

In the above, several variable coefficients must be expanded near the wall. These include asymptotic representations of the Bessel functions in the boundary layer region:

$$\begin{cases} J_0(\lambda_0 x) & \approx 1-\frac{\lambda_0^2x^2}{4}\approx-\left(\frac{\lambda_0^2}{4}-1\right);\quad x=(1-\delta s)\\ J_1(\lambda_0 x) & \approx \frac{\lambda_0 x}{2}-\frac{\lambda_0^3x^3}{16}\approx-\frac{\lambda_0}{2}\left(\frac{\lambda_0^2}{8}-1\right)\\ J_2(\lambda_0 x) & \approx \frac{\lambda_0^2x^2}{8}-\frac{\lambda_0^4x^4}{96}\approx-\frac{\lambda_0^2}{8}\left(\frac{\lambda_0^2}{12}-1\right)\\ J_3(\lambda_0 x) & \approx \frac{\lambda_0^3x^3}{48}-\frac{\lambda_0^5x^5}{768}\approx-\frac{\lambda_0^3}{48}\left(\frac{\lambda_0^2}{16}-1\right)\end{cases} \tag{50}$$

It is clear that the above approximations have no influence on the existing orders. Their backward substitution gives rise to a similar equation to that of Eq. (41), specifically

$$\frac{\mathrm{d}^2\xi_z^{(w)}}{\mathrm{d}s^2}+\alpha\frac{\mathrm{d}\xi_z^{(w)}}{\mathrm{d}s}=0;\qquad \alpha=\frac{\lambda_0}{2\beta J_1(\lambda_0\beta)}\left(\frac{\lambda_0^2}{8}-1\right)\approx 4.91131 \tag{51}$$

This result is not surprising given the physical arguments that compel the axial boundary layer to possess the same character as that of its tangential counterpart, including the form of boundary conditions given by Eq. (43) wherein $\xi_z^{(o)}=\lambda\kappa/[\beta J_1(\lambda\beta)]$. In fact, the solution of Eq. (51) leads to

$$\xi_z^{(w)}=\frac{\lambda_0\kappa}{\beta J_1(\lambda_0\beta)}\left(1-e^{-s\alpha}\right) \tag{52}$$

Finally, upon constructing the composite solution and reverting to the original variables, a uniformly valid axial velocity may be recovered via

$$\xi_z^{(c)}=\xi_z^{(o)}+\xi_z^{(w)}-\lim_{s\to\infty}\xi_z^{(w)}(s) \tag{53}$$

and so

$$u_z^{(c)}=\frac{\lambda_0\kappa z J_0(\lambda_0 r)}{\beta J_1(\lambda_0\beta)}\left\{1-\exp\left[-\frac{\lambda_0 V}{4\pi\beta J_1(\lambda_0\beta)}\left(\frac{\lambda_0^2}{8}-1\right)(1-r)\right]\right\} \tag{54}$$

It may be easily verified that this expression vanishes at the sidewall.

C. Radial Wall Correction

Having incorporated viscous corrections in the tangential and axial directions, the radial velocity has to be adjusted lest continuity is breached. By considering the similarity solutions given by Morgan[38,39] or Blasius,[40] fluid friction

may be seen to exert a tempering effect on u_r to the extent of causing its first derivative to vanish at the wall. While the desired correction may be deduced from the continuity equation, integration leads to special functions and semi-numerical solutions. A more practical route consists of applying similar arguments to those used in handling the axial and tangential momentum equations. Accordingly, the radial boundary layer equation may be expressed as

$$\varepsilon\left(\frac{\partial^2 u_r}{\partial r^2}+\frac{1}{r}\frac{\partial u_r}{\partial r}-\frac{u_r}{r^2}\right)-u_r\frac{\partial u_r}{\partial r}+\frac{u_\theta^2}{r}=\frac{\partial p}{\partial r} \tag{55}$$

In this case, given the small size of the radial contribution, a meaningful approximation may be arrived at when terms of order δ^2 are consistently retained in the momentum equation. When the inviscid pressure is considered, we find

$$\frac{\partial p}{\partial r}=-u_r^{(o)}\frac{\partial u_r^{(o)}}{\partial r}+\frac{1}{r}\left(u_\theta^{(o)}\right)^2=\kappa^2\lambda_0\frac{J_1(\lambda_0 r)}{2\beta^2 J_1^2(\lambda_0\beta)}\left[J_2(\lambda_0 r)-J_0(\lambda_0 r)\right]+\frac{1}{r}\left(u_\theta^{(o)}\right)^2 \tag{56}$$

In the above, the pressure gradient may be eliminated through the use of Prandtl's hypothesis[31] that precludes radial pressure variations across the boundary layer. A conventional asymptotic treatment may also be carried out to justify the dismissal of the pressure gradient. Regardless, the first term on the right-hand-side of Eq. (56) appears at $O(\kappa^2)$, which justifies its removal. By approximating the convective coefficients with their inviscid forms, we put

$$\varepsilon\left(\frac{\partial^2 u_r}{\partial r^2}+\frac{1}{r}\frac{\partial u_r}{\partial r}-\frac{u_r}{r^2}\right)+\kappa\frac{J_1(\lambda_0 r)}{\beta J_1(\lambda_0\beta)}\frac{\partial u_r}{\partial r}=O(\kappa^2) \tag{57}$$

Note that the terms due to the tangential velocity appear on both sides of the equation and therefore cancel identically in Eqs. (56–57).

To permit matching with the outer function, we let $u_r=\xi_r(r)J_1(\lambda_0 r)$. This transformation converts Eq. (57) into

$$\begin{aligned}\varepsilon\Bigg(&\frac{\lambda_0^2}{4}\left[-3J_1(\lambda_0 r)+J_3(\lambda_0 r)\right]\xi_r+\lambda_0\left[J_0(\lambda_0 r)-J_2(\lambda_0 r)\right]\xi_r'+J_1(\lambda_0 r)\,\xi_r''\\&+\frac{1}{r}\left\{\frac{\lambda_0}{2}\left[J_0(\lambda_0 r)-J_2(\lambda_0 r)\right]\xi_r+J_1(\lambda_0 r)\,\xi_r'\right\}-\frac{\xi_r J_1(\lambda_0 r)}{r^2}\Bigg)\\&+\kappa\frac{J_1(\lambda_0 r)}{\beta J_1(\lambda_0\beta)}\left\{\frac{\lambda_0}{2}\left[J_0(\lambda_0 r)-J_2(\lambda_0 r)\right]\xi_r+J_1(\lambda_0 r)\,\xi_r'\right\}=O(\kappa^2)\end{aligned} \tag{58}$$

In the vicinity of the wall, we introduce $s=(1-r)/\delta$ and make use of Eq. (50). After some algebra and rearrangements, a distinguished limit of $\delta\sim\varepsilon/\kappa$ emerges. This enables us to eliminate extraneous terms and write

$$\frac{\mathrm{d}^2\xi_r^{(w)}}{\mathrm{d}s^2}+\alpha\frac{\mathrm{d}\xi_r^{(w)}}{\mathrm{d}s}=0;\qquad\alpha=\frac{\lambda_0}{2\beta J_1(\lambda_0\beta)}\left(\frac{\lambda_0^2}{8}-1\right) \tag{59}$$

As for the boundary conditions, they exhibit the dual form encapsulated by Eq. (43), with the exception of $\xi_r^{(o)}=-\kappa/[\beta J_1(\lambda_0\beta)]$. Solving Eq. (59) results in the straightforward inner approximation

$$\xi_r^{(w)}=-\frac{\kappa}{\beta J_1(\lambda_0\beta)}\left(1-e^{-\alpha s}\right) \tag{60}$$

Subsequently, the corresponding radial velocity may be expressed in terms of the original variables viz.

$$u_r^{(c)}=-\frac{\kappa J_1(\lambda_0 r)}{\beta J_1(\lambda_0\beta)}\left\{1-\exp\left[-\frac{\lambda_0 V}{4\pi\beta J_1(\lambda_0\beta)}\left(\frac{\lambda_0^2}{8}-1\right)(1-r)\right]\right\} \tag{61}$$

IV. Results and Discussion

A vector plot of the linear Beltramian vortex is provided along with the complex-lamellar analog in Fig. 2. For the reader's convenience, a comparison of the linear Beltramian and complex-lamellar models is also furnished in Table 1. It is clear that the two models share similar characteristics and subtle differences. These include the mantle location, where the vectors switch polarity at slightly different points (0.6276 and 0.7071 to be precise), and the speed along the centerline, where the Beltramian model outruns its counterpart. The core and wall boundary layers also appear to be slightly thinner in the Beltramian case. In what follows, the uniformly valid, matched-asymptotic approximation for the velocity will be used to represent the viscous Beltramian profile. For simplicity, the use of a superscript 'c' for 'composite' will henceforth be dropped.

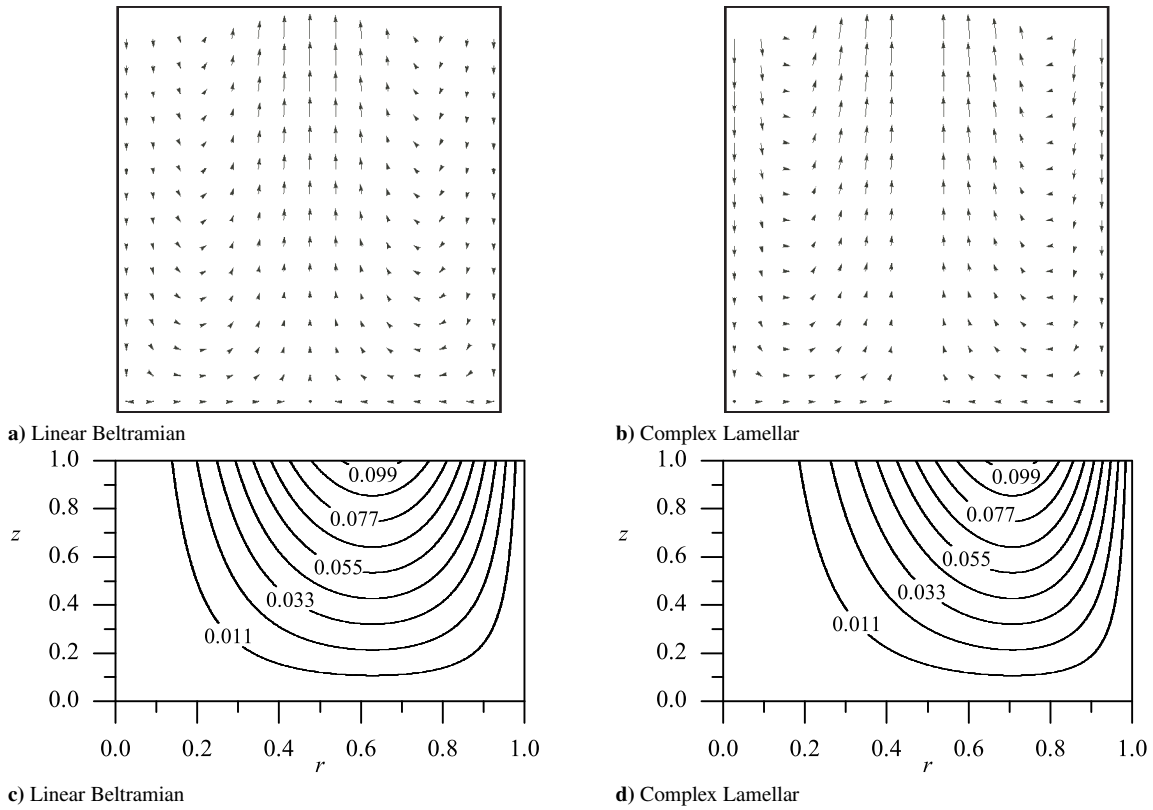

Figure 2. Vector (a,b) and streamline plots (c,d) of the linear Beltramian (left) and complex-lamellar models (right). Unless stated otherwise, we use $\kappa = 0.103$ everywhere.

A. Tangential Velocity Distribution

As shown in Fig. 3, the corrected tangential velocity embodies the effects of viscous stresses around the axis of rotation and along the sidewall. In the core region, fluid friction leads to the onset of a forced vortex that annuls the unbounded character of the swirl velocity which is most pronounced at the origin. The core vortex thus established induces solid body rotation wherein the tangential speed stays directly proportional to the radial distance from the centerline. Near the sidewall, a boundary layer is formed that is highly dependent on the vortex Reynolds number; this dimensionless grouping combines the viscous Reynolds number, swirl number, and the chamber aspect ratio as described in detail by Majdalani and Chiaverini[27] or Maicke and Majdalani.[36]

In Fig. 3a, the swirl velocity is plotted at three different axial stations and one value of $V = 650$. Based on this graph, one ascertains that the swirl velocity is weakly dependent on the axial position. This behavior is slightly different from that of the axially invariant, complex-lamellar solution developed by Vyas and Majdalani.[25] In fact, it is fully consistent with the foregoing assumptions leading to its asymptotic formulation. In contrast, when the vortex Reynolds number is increased from 200 to 800 at fixed $z = 1$, appreciable variations in the velocity profile may be noted, as shown in Fig. 3b. As usual, larger values of V are congruent with diminished viscosity or enhanced injection velocity. At the outset, a shrinking penetration of the boundary layer may be seen to accompany in Fig. 3b the incremental increases in V.

As for the maximum tangential velocity, it may be calculated directly from $\left(u_\theta^{(ci)}\right)' = 0$. Using $r = \delta_c$ to denote the radial position corresponding to the peak tangential value, asymptotic treatment of the radial derivative leads to a weakly z-dependent equation. To good approximation, we set

$$\exp\left[-\frac{r^2 V\lambda_0}{8\pi\beta J_1(\beta\lambda_0)}\right]\left[1+\frac{r^2 V\lambda_0}{4\pi\beta J_1(\beta\lambda_0)}\right] = 1 \tag{62}$$

Table 1. Comparison between the complex-lamellar[27,28] and linear Beltramian models[29]

Complex Lamellar	$\alpha = \frac{1}{6}\pi^2 - 1 \approx 0.644934$	
$u_r = -\frac{\kappa}{r}\sin\left(\pi r^2\right)\left[1 - e^{-\frac{V}{4}\alpha(1-r^2)}\right]$		$(u_r)_{\max} = -1.50573\kappa$
$u_\theta = \frac{1}{r}\left[1 - e^{-\frac{V}{4}r^2} - e^{-\frac{V}{4}\alpha\left(1-r^2\right)}\right]$		$(u_\theta)_{\max} = \frac{\left\{1-\exp\left[\frac{1}{2}+\mathrm{pln}\left(-1,-\frac{1}{2\sqrt{e}}\right)\right]\right\}\sqrt{V}}{\left(1-e^{-\frac{1}{4}V}\right)\sqrt{-1-2\mathrm{pln}\left(-1,-\frac{1}{2\sqrt{e}}\right)}}$
		$\approx 0.3191 V^{1/2}$
$u_z = 2\pi\kappa z\cos\left(\pi r^2\right)\left[1 - e^{-\frac{V}{4}\alpha(1-r^2)}\right]$		$(u_z)_{\max} = 2\pi\kappa z \approx 6.28319\kappa z$
$\delta_c = \sqrt{2V^{-1}\left\{-1 - 2\,\mathrm{pln}\left[-1,-\frac{1}{2}\exp\left(-\frac{1}{2}\right)\right]\right\}} \approx \frac{2.2418}{\sqrt{V}}$		$\delta_w = 1 - \sqrt{1 - \frac{4\ln 100}{\alpha V}} \approx \frac{14.281}{V}$
$\delta_i = 2\sqrt{\frac{\ln 100}{V}} \approx \frac{4.29193}{\sqrt{V}}$		
Linear Beltramian	$\alpha = \frac{\lambda_0}{2\beta J_1(\lambda_0\beta)}\left(\frac{1}{8}\lambda_0^2 - 1\right) \approx 4.91131$	$\gamma = \frac{\lambda_0}{4\beta J_1(\lambda_0\beta)} \approx 2.94002$
$u_r = -\frac{\kappa J_1(\lambda_0 r)}{\beta J_1(\lambda_0\beta)}\left[1 - e^{-\frac{V}{2\pi}\alpha(1-r)}\right] \approx -3.06915\kappa J_1(\lambda_0 r)\left[1 - e^{-\frac{V}{2\pi}\alpha(1-r)}\right]$		$(u_r)_{\max} \approx -1.78489\kappa$
$u_\theta = \frac{1}{r}\left\{\left[1 + \frac{\lambda_0^2\kappa^2 r^2 z^2 J_1^2(\lambda_0 r)}{\beta^2 J_1^2(\lambda_0\beta)}\right]^{1/2} - e^{-\frac{V}{2\pi}\gamma r^2} - e^{-\frac{V}{2\pi}\alpha(1-r)}\right\}$		$(u_\theta)_{\max} \approx \frac{\left\{1-\exp\left[\frac{1}{2}+\mathrm{pln}\left(-1,-\frac{1}{2\sqrt{e}}\right)\right]\right\}\sqrt{\lambda_0 V}}{2\sqrt{\pi\beta J_1(\beta\lambda_0)\left[-1-2\,\mathrm{pln}\left(-1,-\frac{1}{2\sqrt{e}}\right)\right]}}$
		$\approx 0.43654\sqrt{V}$
$u_z = \frac{\lambda_0\kappa z J_0(\lambda_0 r)}{\beta J_1(\lambda_0\beta)}\left[1 - e^{-\frac{V}{2\pi}\alpha(1-r)}\right] \approx 11.7601\kappa z J_0(\lambda_0 r)\left[1 - e^{-\frac{V}{2\pi}\alpha(1-r)}\right]$		$(u_z)_{\max} = 11.7601\kappa z$
$\delta_c \approx 2\sqrt{\frac{\pi\beta J_1(\beta\lambda_0)}{\lambda_0 V}\left[-1 - 2\,\mathrm{pln}\left(-1,-\frac{1}{2\sqrt{e}}\right)\right]} \approx \frac{1.63864}{\sqrt{V}}$		$\delta_w \approx \frac{2\pi}{V\alpha}\ln 100 \approx \frac{5.89153}{V}$
$\delta_i \approx \sqrt{\frac{\beta J_1(\lambda_0\beta)}{2\pi z^2\kappa^2\lambda_0^3}\left(\sqrt{V^2 + 32\pi^2 z^2\kappa^2\lambda_0^2\ln 100} - V\right)} \approx \frac{3.13716}{\sqrt{V}}$		

and extract

$$\delta_c \approx 2\sqrt{\frac{\pi\beta J_1(\beta\lambda_0)}{\lambda_0 V}\left[-1 - 2\,\mathrm{pln}\left(-1,-\frac{1}{2\sqrt{e}}\right)\right]} \approx \frac{1.63864}{\sqrt{V}} \tag{63}$$

where, for simplicity, the axial dependence is ignored. Interestingly, the characteristic radius of the forced vortex is nearly 73.1% of its value in the complex-lamellar case. Forthwith, Eq. (63) enables us to estimate the maximum swirl velocity from

$$(u_\theta)_{\max} \approx \frac{1 - e^{\frac{1}{2}+\mathrm{pln}\left(-1,-\frac{1}{2\sqrt{e}}\right)}}{2\sqrt{\pi\beta J_1(\beta\lambda_0)\left[-1 - 2\,\mathrm{pln}\left(-1,-\frac{1}{2\sqrt{e}}\right)\right]}}\sqrt{\lambda_0 V} \approx 0.43654\sqrt{V} \tag{64}$$

Recalling that the complex-lamellar model entails a maximum speed of $0.3191\sqrt{V}$, the present solution is seen to be roughly 36.8% faster.

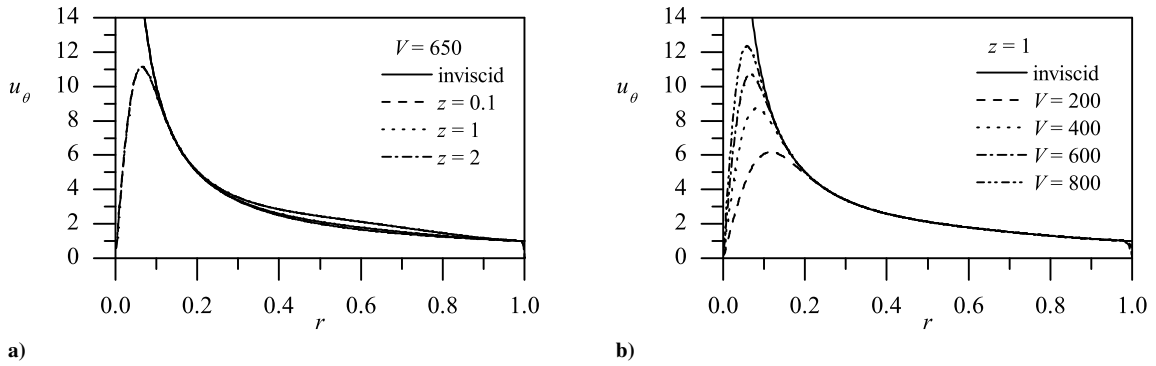

Figure 3. Tangential velocity plots showing effects of a) axial variations and b) sequentially increasing V.

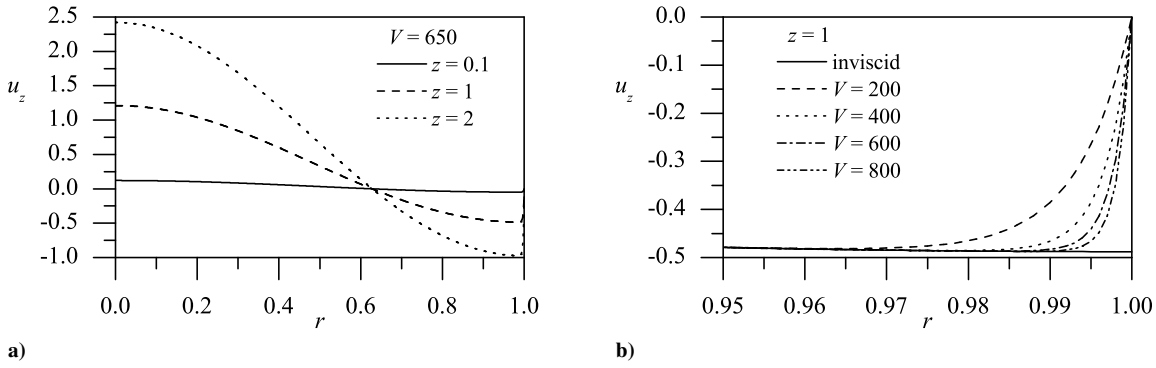

Figure 4. Axial velocity plots showing effects of a) axial variations and b) sequentially increasing V at $z = 1$.

B. Axial Velocity Distribution

As shown in Fig. 4, the amended axial velocity is capable of sensing the frictional effects that become progressively more pronounced in the close vicinity of the wall. The matched-asymptotic approximation for u_z is clearly observant of the no-slip requirement at the sidewall. In this vein, Fig. 4a illustrates the linear dependence of the solution on the axial position, which is taken at $z = 0.1, 1$ and 2, where z represents the normalized distance from the headwall. Although not shown, we find $u_z = 0$ at the headwall where no flow is permitted. Then recalling that the original solution is linearly dependent on z, we continue to observe larger axial velocities at progressively larger distances from the headwall. Conversely, Fig. 4b details the dependence of the boundary layer profile on the vortex Reynolds number. As with the tangential velocity, we recognize a strong dependence on V. The limiting case of $V \to 0$ corresponds to a vanishing inflow parameter, $\kappa \to 0$. Naturally, the absence of a mean inflow velocity causes the solution to categorically vanish. On the other hand, we can see from Fig. 4b that as the vortex Reynolds number increases, the boundary layer thickness decreases, and the solution shifts toward its inviscid form. Mathematically, this observation can be confirmed by setting $V = \infty$ in Eq. (54) whence the inviscid motion may be restored.

Along the centerline, the maximum speed may be written as

$$(u_z)_{\max} = u_z(0, z) = \frac{\lambda_0 \kappa z J_0(0)}{\beta J_1(\lambda_0 \beta)} \left\{ 1 - \exp\left[-\frac{\lambda_0 V}{4\pi\beta J_1(\lambda_0 \beta)} \left(\frac{\lambda_0^2}{8} - 1 \right) \right] \right\} \approx 11.7601 z\kappa \tag{65}$$

This peak value is 87.2% larger than the maximum centerline speed, $2\pi\kappa z$, associated with the sinusoidal profile.[27]

C. Radial Velocity Distribution

We recall that the equation from which the wall correction is derived for u_r does not exclude second order terms in δ. This assumption was previously tested by Batterson and Majdalani.[28] Although we retain the mathematical form

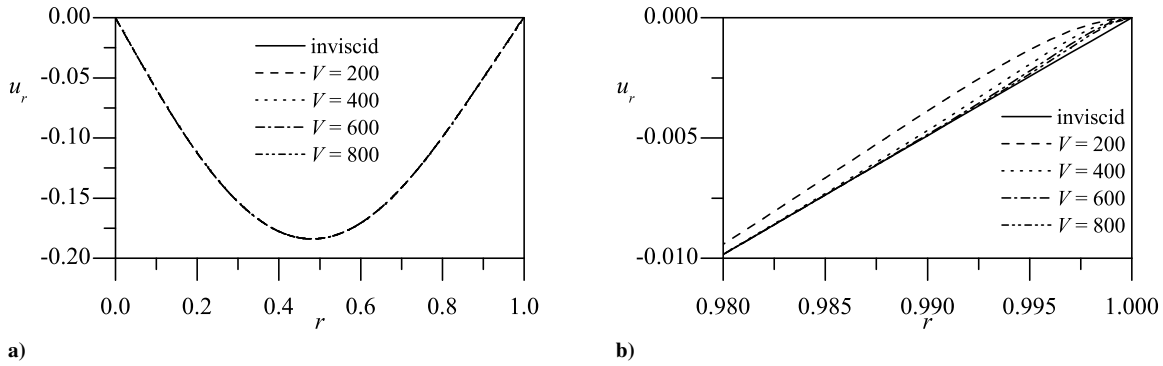

Figure 5. Variation of u_r with successive increases in V shown over a) the entire chamber radius and b) the thin viscous region.

entailed in both tangential and axial boundary layer equations, the graphical representation in Fig. 5a confirms the nearly insignificant spatial influence of viscosity on the radial velocity. The magnification granted by Fig. 5b shifts our attention to the thin viscous region where a smoothing effect appears in the radial velocity curvature, particularly, as u_r and its derivative approach zero at the end of the domain. This effect is further corroborated by the numerical work of Morgan,[38,39] Blasius,[40] and others. From a practical standpoint, the end-of-interval rounding can be shown to mainly affect the shear stress calculation at the sidewall.

D. Boundary Layer Thickness

Following Prandtl's convention, the boundary layer thickness δ may be taken as the distance necessary to recover 99% of the outer solution. This definition can be applied to both the inner core and sidewall regions. However, it must be borne in mind that the width of the core vortex is traditionally taken as twice the distance, δ_c, from the axis of rotation to the point where the tangential velocity reaches its maximum. This quantity is also representative of the inner boundary layer. Since δ_c is already given by Eq. (63), we now embark on the calculation of the 99% viscous core layer, δ_i. To this end, we consider Eq. (36) and exclude the tangential sidewall corrections insofar as they exert no influence on the core region. After proper substitutions, we arrive at a transcendental equation for δ_i that requires numerical root solving viz.

$$-\frac{V}{2\pi}\gamma r^2 = \ln\left[\frac{1}{100}\left(1+\frac{\lambda_0^2\kappa^2 r^2 z^2 J_1^2(\lambda_0 r)}{\beta^2 J_1^2(\lambda_0\beta)}\right)^{1/2}\right] \tag{66}$$

To circumvent the need for numerical computation, we expand the preceding equation into a Taylor series from which a one-term expression may be retained. This is subsequently used to extract a closed-form approximation for the radial position corresponding to the edge of the core layer. We find

$$\delta_i \approx \sqrt{\frac{\beta J_1(\lambda_0\beta)}{2\pi z^2\kappa^2\lambda_0^3}\left(\sqrt{V^2+32\pi^2 z^2\kappa^2\lambda_0^2\ln(100)}-V\right)} \approx 4\sqrt{\frac{\pi\beta J_1(\lambda_0\beta)\ln 10}{\lambda_0 V}} \approx \frac{3.13716}{\sqrt{V}} \tag{67}$$

so that $\delta_i/\delta_c \approx 1.91449$. Interestingly, this solution displays a secondary dependence on the axial location z. Moreover, the edge of the core layer appears at a radial position just under twice that of the maximum velocity. This behavior is characteristic of swirl-dominated motions for which the core vortex diameter is often taken as twice the radial distance from the centerline to the point where the tangential velocity reaches its peak. In comparison, the diameter of the forced vortex is merely 4.5% larger than Prandtl's 99%-based boundary layer thickness δ_i.

On the opposite side of the domain, the sidewall boundary layer, δ_w, may be found by calculating the distance between the radial position where the solution reaches 99% of the inviscid value and the normalized chamber radius. By limiting our attention to the local correction in u_θ, the edge of the wall boundary layer may be estimated from the transcendental equation

$$-\frac{V}{2\pi}\alpha(1-r) = \ln\left[\frac{1}{100}\left(1+\frac{\lambda_0^2\kappa^2 r^2 z^2 J_1^2(\lambda_0 r)}{\beta^2 J_1^2(\lambda_0\beta)}\right)^{1/2}\right] \tag{68}$$

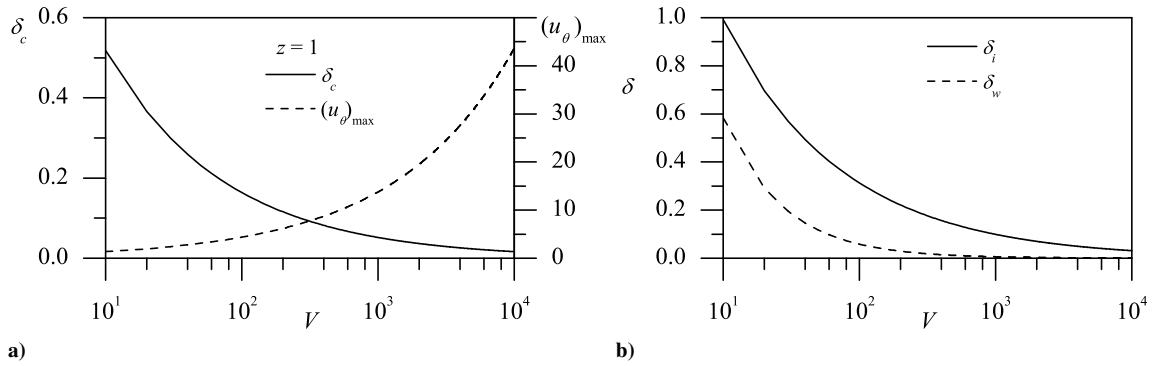

Figure 6. Effect of increasing V on a) the forced vortex core thickness δ_c with its peak tangential velocity, and b) Prandtl's inner core and sidewall boundary layers.

Table 2. Prandtl's inner core and sidewall boundary layer thicknesses at different positions and vortex Reynolds numbers

	Inner boundary layer, δ_i					Sidewall boundary layer, δ_w				
z	$V = 200$	$V = 400$	$V = 600$	$V = 800$	$V = 1000$	$V = 200$	$V = 400$	$V = 600$	$V = 800$	$V = 1000$
0.0	0.2218	0.1569	0.1281	0.1109	0.0992	0.0295	0.0147	0.0098	0.0074	0.0059
0.5	0.2218	0.1569	0.1281	0.1109	0.0992	0.0295	0.0147	0.0098	0.0074	0.0059
1.0	0.2217	0.1568	0.1281	0.1109	0.0992	0.0294	0.0147	0.0098	0.0074	0.0059
1.5	0.2215	0.1568	0.1281	0.1109	0.0992	0.0294	0.0147	0.0098	0.0074	0.0059
2.0	0.2213	0.1568	0.1280	0.1109	0.0992	0.0294	0.0147	0.0098	0.0074	0.0059

Note that $\delta_w = 1-r$, where r refers to the edge of the wall layer. From the one-term Taylor series expansion of Eq. (68), a compact expression may be arrived at, namely,

$$\delta_w = 1 - r \approx \frac{2\pi}{V\alpha} \ln(100) \tag{69}$$

It is clear that the use of a one-term Taylor-series approximation renders the boundary layer thickness axially invariant. However, when taking into account the range of reported results, we find a less than 0.2% maximum difference between Eqs. (68) and (69). Applying the same boundary layer analysis to either the axial or radial velocity profiles leads to an identical result to that of Eq. (69). This outcome may be viewed as self-conforming in all three directions, being asymptotically equivalent to Eq. (68). The minor disparity observed may be attributed to the subtle differences in the pathways through which the r, θ and z momentum equations are converted and reduced into their inner boundary layer expressions.

By way of comparison, we provide in Fig. 6 a characterization of the three boundary layers, δ_c, δ_i, and δ_w, along with the maximum tangential velocity, $(u_\theta)_{\max}$, as a function of V. The corresponding graphs are given at fixed axial position and show, in Fig. 6a, the peak velocity and its radial location, and in Fig. 6b, a side-by-side comparison of the inner core and sidewall boundary layers. We note in this respect that Prandtl's boundary layer thickness at the core is the largest, being simply $1.9145\delta_c$ and $0.5325\sqrt{V}\delta_w$. More explicit numerical values are furnished in Table 2 where δ_i and δ_w are produced from their exact expressions at several axial positions and $V = 200, 400, \ldots, 1000$. From this table, it may be seen that axial variations in the boundary layer remain negligible. For the reader's convenience, the various approximations obtained heretofore are catalogued in Table 1.

E. Pressure Distribution

Based on Eq. (7), we can calculate both the radial and axial pressure gradients. To good approximation, we find

$$\frac{\partial p}{\partial r} \approx r^{-3}\left[1 + e^{-\frac{V}{\pi}\gamma r^2} + e^{-\frac{V}{\pi}\alpha(1-r)} - 2e^{-\frac{V}{2\pi}\gamma r^2} - 2e^{-\frac{V}{2\pi}\alpha(1-r)}\right] + \frac{z^2\kappa^2\lambda_0^2 J_1^2(\lambda_0 r)}{r\beta^2 J_1(\lambda_0\beta)} \tag{70}$$

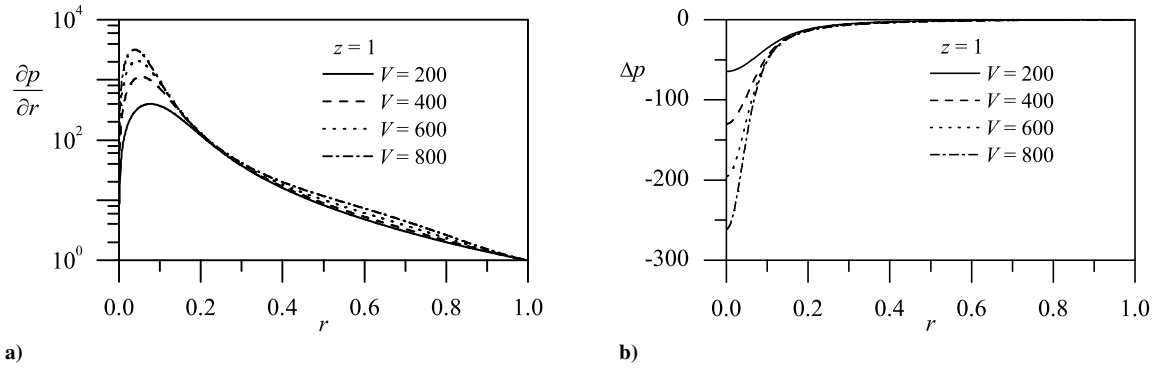

Figure 7. Variation of a) the radial pressure gradient and b) the pressure with successive increases in V.

The radial gradient of pressure is shown in Fig. 7a. The profile mirrors that of the tangential velocity that has a bearing on the pressure gradient by virtue of its centripetal action (i.e., u_θ^2/r). The largest magnitude in $\partial p/\partial r$ seems to occur near the point of maximum swirl velocity

$$\delta_p \approx 1.0484 V^{-1/2} \tag{71}$$

Then using $p_0 = p_0(1, 0)$, we introduce the pressure differential as $\Delta p = p - p_0$. Upon integration, the radial pressure gradient yields

$$\begin{aligned}
\Delta p\,(r,z) = \frac{r^2-1}{2r^2} + \frac{1}{2}e^{-\frac{V}{\pi}\gamma} - e^{-\frac{V}{2\pi}\gamma} + \frac{1}{r^2}\left(e^{-\frac{V}{2\pi}\gamma r^2} - \frac{1}{2}e^{-\frac{V}{\pi}\gamma r^2}\right) \\
+ \frac{V}{2\pi}\gamma\left[\mathrm{Ei}\left(-\frac{V}{\pi}\gamma\right) - \mathrm{Ei}\left(-\frac{V}{\pi}\gamma r^2\right) + \mathrm{Ei}\left(-\frac{V}{2\pi}\gamma r^2\right) - \mathrm{Ei}\left(-\frac{V}{2\pi}\gamma\right)\right] \\
+ \frac{1}{2} + \frac{V}{2\pi}\alpha - \frac{V^2}{2\pi^2}\alpha^2\mathrm{Ei}\left(\frac{V}{\pi}\alpha\right)e^{-\frac{V}{\pi}\alpha} \\
+ \frac{1}{2r^2\varepsilon^2}\left(-e^{-\frac{V}{\pi}\alpha(1-r)}\varepsilon\,(\varepsilon + 2r\alpha\kappa) + 4r^2\alpha^2\kappa^2 e^{-\frac{V}{\pi}\alpha}\mathrm{Ei}\left(\frac{V}{\pi}\alpha r\right)\right) \\
- \frac{4\pi^2\kappa^2 + 2\pi\alpha V\kappa^2 - \alpha^2\kappa^2\mathrm{Ei}\left(\frac{V}{2\pi}\alpha\right)e^{-\frac{V}{2\pi}\alpha}}{4\pi^2\kappa^2} \\
+ \frac{\left(4\pi^2\kappa^2 + 2\pi V\kappa^2\alpha r\right)e^{-\frac{V}{2\pi}\alpha(1-r)} - r^2V^2\alpha^2\kappa^2 e^{-\frac{V}{2\pi}\alpha}\mathrm{Ei}\left(\frac{V}{2\pi}\alpha r\right)}{4\pi^2\kappa^2 r^2} \\
+ \frac{z^2\kappa^2\lambda_0^2}{2\beta^2 J_1(\lambda_0\beta)}\left[J_0^2(\lambda_0) - J_0^2(\lambda_0 r) + J_1^2(\lambda_0) - J_1^2(\lambda_0 r)\right]
\end{aligned} \tag{72}$$

Likewise, the axial gradient may be expressed as,

$$\begin{aligned}
\frac{\partial p}{\partial z} = -\frac{z\kappa^2\lambda_0}{2\pi\beta^2 J_1^2(\lambda_0\beta)}\left(1 - e^{-\frac{V}{2\pi}\alpha(1-r)}\right) \\
\times\left\{2\pi\lambda_0\left[J_0^2(\lambda_0 r) + J_1^2(\lambda_0 r)\right] - e^{-\frac{V}{2\pi}\alpha(1-r)}\left[2\pi\lambda_0 J_0^2(\lambda_0 r) - V\alpha J_0(\lambda_0 r)J_1(\lambda_0 r) + 2\pi\lambda_0 J_1^2(\lambda_0 r)\right]\right\}
\end{aligned} \tag{73}$$

then integrated in the axial direction to obtain,

$$\begin{aligned}
\Delta p(r,z) = -\frac{z^2\kappa^2\lambda_0}{4\pi\beta^2 J_1^2(\lambda_0\beta)}\left(1 - e^{-\frac{V}{2\pi}\alpha(1-r)}\right) \\
\times\left\{2\pi\lambda_0\left[J_0^2(\lambda_0 r) + J_1^2(\lambda_0 r)\right] - e^{-\frac{V}{2\pi}\alpha(1-r)}\left[2\pi\lambda_0 J_0^2(\lambda_0 r) - V\alpha J_0(\lambda_0 r)J_1(\lambda_0 r) + 2\pi\lambda_0 J_1^2(\lambda_0 r)\right]\right\}
\end{aligned} \tag{74}$$

It may be helpful to note that, unlike the inviscid solution for which a unified expression for the pressure may be readily obtained,[29] the differential for the pressure here is not exact. As a result, the mixed partials for p are not

commutative and, as such, do not meet the integrability criteria described by Saad and Majdalani.[41] Therefore, given the asymptotic nature of the present formulation, evaluation of the pressure will depend on the path of integration. It can be obtained, for example, along a constant r or z. For pressure variations along the centerline, one may integrate the pressure gradient in the axial direction before setting $r = 0$. While such deficiency may be detrimental to the pressure evaluation in some physical settings, it proves inconsequential to the problem at hand. This may be ascribed to the relatively short length of chambers in which bidirectional vortex motion may be sustained. In such situations, contributions from axial gradients can be several orders of magnitude smaller than those associated with the radial pressure gradient. Consequently, the pressure given by Eq. (72) may be viewed as a reasonable representation of the total pressure field. This behavior is exemplified in Fig. 7b where the pressure distribution across the chamber diameter is plotted for $z = 1$ and $V = 200, 400, 600, 800$. This graph is quite illuminating as it displays a large pressure drop near the core where a low pressure region is created. Such a local vacuum leads to a negative crossflow velocity that helps to draw the fluid entrained in the outer annulus into the inner vortex.

F. Vorticity Distribution

The vorticity profile may be evaluated from

$$\boldsymbol{\omega} = \nabla \times \boldsymbol{u} = -\frac{\partial u_\theta}{\partial z}\boldsymbol{e}_r + \left(\frac{\partial u_r}{\partial z} - \frac{\partial u_z}{\partial r}\right)\boldsymbol{e}_\theta + \left(\frac{\partial u_\theta}{\partial r} + \frac{u_\theta}{r}\right)\boldsymbol{e}_z \tag{75}$$

Although this study is focused on the boundary layers of Eq. (25), it may be worthwhile to compare our results to those associated with the complex-lamellar model.[27] While functionally different, only minor differences may be detected in the shape and amplitude of their velocities and pressure profiles. In hindsight, the most characteristic feature of the Beltramian solution and, what sets it apart, stands, perhaps, in its vorticity character. Whereas the complex-lamellar solution can only engender one component of vorticity, $\omega_\theta = 4\pi^2\kappa r z \sin(\pi r^2)$, the axially dependent tangential velocity here gives rise to a fully three-dimensional vorticity formulation. This was calculated by Majdalani[29] and written as

$$\boldsymbol{\omega} = -\frac{rz\kappa^2{\lambda_0}^2{J_1}^2(\lambda_0 r)}{\beta^2 J_1(\lambda_0\beta)\sqrt{1+\frac{r^2z^2\kappa^2{\lambda_0}^2{J_1}^2(\lambda_0 r)}{\beta^2 J_1(\lambda_0\beta)}}}\boldsymbol{e}_r + \frac{z\kappa\lambda_0^2 J_1(\lambda_0 r)}{\beta J_1(\lambda_0\beta)}\boldsymbol{e}_\theta + \frac{rz^2\kappa^2{\lambda_0}^3 J_0(\lambda_0 r)J_1(\lambda_0 r)}{\beta^2 J_1(\lambda_0\beta)\sqrt{1+\frac{r^2z^2\kappa^2{\lambda_0}^2{J_1}^2(\lambda_0 r)}{\beta^2 J_1(\lambda_0\beta)}}}\boldsymbol{e}_z \tag{76}$$

This result suggests a vanishing Lamb vector through which the main source of nonlinearity is removed. By considering the ratio between vorticity and velocity, a simple relationship emerges via

$$\frac{\boldsymbol{\omega}}{\boldsymbol{u}} = \lambda_0\left[1+\frac{\beta^2 J_1^2(\lambda_0\beta)}{\kappa^2\lambda_0^2 r^2 z^2 J_1^2(\lambda_0 r)}\right]^{-1/2} \tag{77}$$

Had this ratio been constant, it would have implied a Trkalian subclass of Beltramian flows. On this note, we find Trkalian flows to be mathematically feasible but not physically plausible in the modeling of bidirectional vortex motions.[29] Their viscous treatment is hence excluded. In contrast, the original solution by Vyas and Majdalani[25] is seen to belong to a family of complex-lamellar flows for which the vorticity and velocity vectors remain orthogonal. This property, namely $\boldsymbol{\omega}\cdot\boldsymbol{u} = 0$, causes streamlines and vorticity lines to remain perpendicular everywhere.

With the inclusion of viscous corrections Eq. (75) becomes

$$\begin{aligned}\boldsymbol{\omega} = &-\frac{rz\kappa^2\lambda_0^2 J_1^2(\lambda_0 r)}{\beta^2 J_1(\lambda_0\beta)\sqrt{1+\frac{r^2z^2\kappa^2\lambda_0^2 J_1^2(\lambda_0 r)}{\beta^2 J_1(\lambda_0\beta)}}}\boldsymbol{e}_r \\ &+\frac{z\kappa\lambda_0}{\beta J_1(\lambda_0\beta)}\left[\frac{V}{2\pi}\alpha J_0(\lambda_0 r)e^{-\frac{V}{2\pi}\alpha(1-r)} + \lambda_0 J_1(\lambda_0 r)\left(1-e^{-\frac{V}{2\pi}\alpha(1-r)}\right)\right]\boldsymbol{e}_\theta \\ &+\frac{V}{2\pi}\left(2\gamma e^{-\frac{V}{2\pi}\gamma r^2} - r^{-1}e^{-\frac{V}{2\pi}\alpha(1-r)}\right) + \frac{rz^2\kappa^2\lambda_0^3 J_0(\lambda_0 r)J_1(\lambda_0 r)}{\beta^2 J_1(\lambda_0\beta)\sqrt{1+\frac{r^2z^2\kappa^2\lambda_0^2 J_1^2(\lambda_0 r)}{\beta^2 J_1(\lambda_0\beta)}}}\boldsymbol{e}_z\end{aligned} \tag{78}$$

At this point, we may take the Pythagorean sum of the vorticity vector to retrieve an expression for the total magnitude

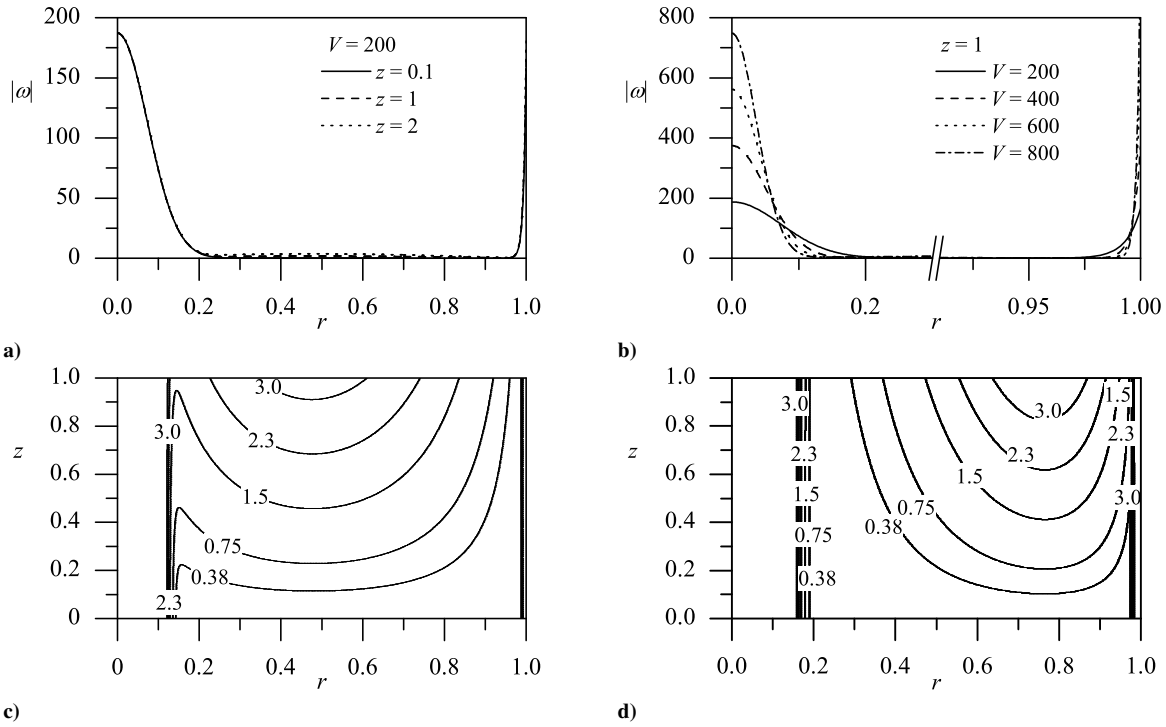

Figure 8. Vorticity plots showing effects of a) axial variations and b) sequentially increasing V. Part c) graphically compares constant vorticity lines of the Beltramian vortex with d) the complex-lamellar model. [27]

of vorticity. We get,

$$|\omega| \approx \left\{ \begin{array}{l} r^{-2}\left[\dfrac{V}{2\pi}\left(2r\gamma e^{-\frac{V}{2\pi}\gamma r^2} - \alpha e^{-\frac{V}{2\pi}\alpha(1-r)}\right) + \dfrac{r^2 z^2 \kappa^2 \lambda_0^3 J_0(\lambda_0 r) J_1(\lambda_0 r)}{\beta^2 J_1(\lambda_0\beta)\sqrt{1+\frac{r^2 z^2 \kappa^2 \lambda_0^2 J_1^2(\lambda_0 r)}{\beta^2 J_1(\lambda_0\beta)}}}\right] \\ + \dfrac{V\kappa z^2 \lambda_0^2}{4\pi^2\beta^2 J_1^2(\lambda_0\beta)}\left[2\pi\lambda_0 J_1(\lambda_0 r) + e^{-\frac{V}{2\pi}\alpha(1-r)}\left(V\alpha J_0(\lambda_0 r) - 2\pi\lambda_0 J_1(\lambda_0 r)\right)\right]^2 \end{array} \right\}^{1/2} \tag{79}$$

where transcendental terms are dismissed. This solution is illustrated in Fig. 8 where the sensitivity of $|\omega|$ is explored vis-à-vis variations in z, V and r. For example, when axial variations are taken into account, it may be inferred from Fig. 8a that the effect of z is strongly limited to the bulk, inviscid flow region. Conversely, typical excursions in the vortex Reynolds number, such as those depicted in Fig. 8b, seem to affect the core and wall boundary layer regions almost exclusively. To put matters into broader perspective, Figs. 8c–8d compare the Beltramian and complex-lamellar isovorticity lines. Both exhibit an increase in vorticity along the length of the chamber. However, the vorticity in the Beltramian model penetrates deeper inwardly and persists closer to the centerline. The nearly vertical isovorticity lines that may be seen near centerline and sidewall regions may be attributed to the nearly constant-thickness boundary layers. At both ends of the domain, these lines represent the essentially vertical boundaries separating the predominantly inviscid, bulk fluid motion, and the viscous-dominated core and sidewall regions.

V. Conclusions

In this study, we manage to obtain an asymptotic formulation to the linear Beltramian profile that arises in the context of confined cyclonic motion in a cylindrical chamber. In this effort, the base flow, which is derived from first principles,[29] is taken to represent the outer field. After re-sketching the inviscid model, we convert the tangential momentum equation and use matched-asymptotic expansion theory to capture the forced vortex layer forming around the axis of rotation. Another wall-coordinate transformation is employed to resolve the frictional forces acting along the circumferential walls. Erdélyi's concept of composite matching is then used to combine the dual endpoint boundary

layer solutions into one, uniformly valid expression. The procedure needed to secure the no slip requirement at the wall is systematically repeated in both axial and radial directions. At the outset, small viscous corrections are incorporated into the axial and radial velocities to the extent that a uniformly valid vector field is obtained in which all singularities are suppressed. The procedure followed to reduce the Navier-Stokes system into a scalar set of suitably scaled inner boundary layer equations involves both independent and dependent-variable transformations. The latter are needed to remove spatial dependence in the far-field boundary and hence permit matching to occur between inner and outer representations.

Based on the present formulation, estimates for the forced vortex core thickness and rotational speed are provided alongside the boundary layers forming above the sidewall in all three spatial directions. In the same vein, the loci of maximum tangential, axial, and radial velocities are identified and the peak magnitude in each direction is separately ascertained. Pressure and vorticity variations are also assessed and compared to each of their sinusoidal, complex-lamellar counterparts.[27,28] The pressure analysis is carried out asymptotically due to the inability to obtain an exact pressure differential. This limitation is overcome by disregarding the higher-order influence of the axial pressure gradient and integrating for the pressure distribution in the radial direction while fixing z. This strategy is fully justified by virtue of the relatively short chambers associated with bidirectional vortex applications. Evidently, the prevailing terms are those connected with the swirl velocity and its centripetal action. This action leads to a suction field in the core region that helps to attract the fluid originating from the annular vortex. Terms connected with the axial and radial velocities or their derivatives appear at order κ^2 and may hence be discarded.

Overall, we find all velocities associated with the linear Beltramian profile to exceed those of the complex-lamellar model. In contrast, the size of all boundary layers is seen to be proportionately smaller here due to the overall enhancement in speed. As usual, most physically interesting flow features are determined as function of a vortex Reynolds number V. This dimensionless group combines the effects of the Reynolds number, chamber aspect ratio, and swirl number.

As for the vorticity distribution, it resembles its affiliate with the complex-lamellar model. However, the Beltramian vorticity possesses nonzero components in all three directions; it occupies a larger portion of the chamber volume to the extent that constant vorticity lines extend much farther laterally in a given cross-section. In practice, such a pattern is likely to promote the onset of turbulence. Furthermore, the corresponding isovorticity lines differ from those that accompany Rankine's irrotational vortex owing to their secondary dependence on the axial coordinate over their inviscid segment.

Acknowledgments

This project was completed with support from the National Science Foundation through Grant No. CMMI-0928762, Dr. Eduardo A. Misawa, Program Director.

References

[1]Penner, S. S., "Elementary Considerations of the Fluid Mechanics of Tornadoes and Hurricanes," *Acta Astronautica*, Vol. 17, 1972, pp. 351–362.

[2]Königl, A., "Stellar and Galactic Jets: Theoretical Issues," *Canadian Journal of Physics*, Vol. 64, No. 4, 1986, pp. 362–368. doi:10.1139/p86-063.

[3]Bruce, C., "Spiral Stellar Nebulae and Cosmic Gas Jets," *Journal of the Franklin Institute*, Vol. 271, No. 1, 1961, pp. 1–11. doi:10.1016/s0016-0032(61)91011-0.

[4]Vatistas, G. H., *Vortices in Homer's Odyssey – a Scientific Approach*, Vol. 6 of *History of Mechanism and Machine Science*, Springer, The Netherlands, 2009, pp. 67–75. doi:10.1007/978-1-4020-8784-4_4.

[5]Rankine, W., *A Manual of Applied Mechanics*, Griffin, 1877.

[6]Trapp, R. J., "A Clarification of Vortex Breakdown and Tornadogenesis," *Monthly Weather Review*, Vol. 128, No. 3, March 01 2000, pp. 888–895. doi:10.1175/1520-0493(2000)128<0888:ACOVBA>2.0.CO;2.

[7]Kurosaka, M., "Acoustic Streaming in Swirling Flow and the Ranque-Hilsch (Vortex-Tube) Effect," *Journal of Fluid Mechanics*, Vol. 124, No. 1, November 1982, pp. 139–172. doi:10.1017/S0022112082002444.

[8]Wu, J., "Conical Turbulent Swirling Vortex with Variable Eddy Viscosity," *Proceedings of the Royal Society of London. Series A*, Vol. 403, No. 1825, 1986, pp. 235–268. doi:10.1098/rspa.1986.0011.

[9]Ashill, P. R., Fulker, J. L., and Hackett, K. C., "Studies of Flows Induced by Sub Boundary Layer Vortex Generators (SBVGs)," *40th AIAA Aerospace Sciences Meeting and Exhibit*, AIAA Paper 2002-968, Reno, Nevada, Jan. 2002.

[10]Di Cicca, G. M., and Iuso, G., "On Large-Scale Vortical Structures Produced by a Yawed Synthetic Jet-Turbulent Boundary Layer Interaction," *3rd AIAA Flow Control Conference*, AIAA Paper 2006-2861, San Francisco, California, June 2006.

[11]Lamb, H., *Hydrodynamics*, Dover Publications, 1932.

[12]Oseen, C. W., "Über Wirbelbewegung in Einer Reibenden Flüssigkeit," *Arkiv foer Matematik, Astronomi, och Fysik*, Vol. 7, 1911, pp. 1–13.

[13]Burgers, J., "A Mathematical Model Illustrating the Theory of Turbulence," *Advances in Applied Mechanics*, Vol. 1, 1948, pp. 171–199. doi:10.1016/S0065-2156(08)70100-5.

[14]Burgers, J. M., "On the Resistance of Fluids and Vortex Motion," *Koninklijke Nederlandsche Akademie van Wetenschappen Proceedings*, Vol. 23, No. 1, 1921, pp. 774–782.

[15]Rott, N., "Boundary Layers and their Interactions in Rotating Flows," *Progress in Aerospace Sciences*, Vol. 7, 1966, pp. 111–144. doi:10.1016/0376-0421(66)90007-8.

[16]Rott, N., "On the Viscous Core of a Line Vortex," *Zeitschrift für Angewandte Mathematik und Physik (ZAMP)*, Vol. 9, No. 5, 1958, pp. 543–553. doi:10.1007/BF02424773.

[17]Batterson, J. W., Maicke, B. A., and Majdalani, J., "Advancements in Theoretical Models of Confined Vortex Flowfields," *2007 JANNAF Propulsion Conference*, JANNAF Paper TP-2007-222, Denver, Colorado, May 2007.

[18]Eloy, C., and Le Dizès, S., "Three-Dimensional Instability of Burgers and Lamb-Oseen Vortices in a Strain Field," *Journal of Fluid Mechanics*, Vol. 378, 1999, pp. 145–166. doi:10.1017/S0022112098003103.

[19]Sullivan, R., "A Two-Cell Vortex Solution of the Navier-Stokes Equations," *Journal of Aerospace Sciences*, Vol. 26, 1959, pp. 767–768.

[20]Bloor, M., and Ingham, D., "The Flow in Industrial Cyclones," *Journal of Fluid Mechanics*, Vol. 178, 1987, pp. 507–519. doi:10.1017/S0022112087001344.

[21]Barber, T. A., and Majdalani, J., "Exact Eulerian Solution of the Conical Bidirectional Vortex," *45th AIAA/ASME/SAE/ASEE Joint Propulsion Conference and Exhibit*, AIAA Paper 2009-5306, Denver, Colorado, Aug. 2009.

[22]Gloyer, P. W., Knuth, W. H., and Goodman, J., "Overview of Initial Research into the Effects of Strong Vortex Flow on Hybrid Rocket Combustion and Performance," *CSTAR Fifth Annual Symposium*, Paper N96-16953, Tullahoma, Tennessee, Jan. 1993.

[23]Knuth, W., Chiaverini, M., Sauer, J., and Gramer, D., "Solid-Fuel Regression Rate Behavior of Vortex Hybrid Rocket Engines," *Journal of Propulsion and Power*, Vol. 18, No. 3, 2002, pp. 600–609. doi:10.2514/2.5974.

[24]Chiaverini, M., Malecki, M., Sauer, J., Knuth, W., and Majdalani, J., "Vortex Thrust Chamber Testing and Analysis for O2-H2 Propulsion Applications," *39th AIAA/ASME/SAE/ASEE Joint Propulsion Conference and Exhibit*, AIAA Paper 2003-4473, Huntsville, Alabama, July 2003.

[25]Vyas, A., and Majdalani, J., "Exact Solution of the Bidirectional Vortex," *AIAA Journal*, Vol. 44, No. 10, 2006, pp. 2208. doi:10.2514/1.14872.

[26]Majdalani, J., and Rienstra, S., "On the Bidirectional Vortex and Other Similarity Solutions in Spherical Coordinates," *Journal of Applied Mathematics and Physics (ZAMP)*, Vol. 58, No. 2, 2007, pp. 289–308. doi:10.1007/s00033-006-5058-y.

[27]Majdalani, J., and Chiaverini, M. J., "On Steady Rotational Cyclonic Flows: The Viscous Bidirectional Vortex," *Physics of Fluids*, Vol. 21, No. 10, 2009, pp. 103603. doi:10.1063/1.3247186.

[28]Batterson, J. W., and Majdalani, J., "Sidewall Boundary Layers of the Bidirectional Vortex," *Journal of Propulsion and Power*, Vol. 26, No. 1, 2009, pp. 102–112. doi:10.2514/1.40442.

[29]Majdalani, J., "Exact Eulerian Solutions of the Cylindrical Bidirectional Vortex," *45th AIAA/ASME/SAE/ASEE Joint Propulsion Conference and Exhibit*, AIAA Paper 2009-5307, Denver, Colorado, Aug. 2009.

[30]Wu, J., Ma, H., and Zhou, M., *Vorticity and Vortex Dynamics*, Springer, New York, New York, 2006.

[31]Prandtl, L., "Zur Berechnung der Grenzschichten," *Zeitschrift für angewandte Mathematik und Mechanik (ZAMM)*, Vol. 18, No. 1, 1938, pp. 77–82. doi:10.1002/zamm.19380180111.

[32]Bragg, S. L., and Hawthorne, W. R., "Some Exact Solutions of the Flow Through Annular Cascade Actuator Discs," *Journal of the Aeronautical Sciences*, Vol. 17, 1950, pp. 243.

[33]Nayfeh, A. H., *Perturbation Methods*, Wiley, New York, 1973.

[34]Erdélyi, A., *Asymptotic Expansions*, Dover publications, New York, 1956.

[35]Majdalani, J., "Vortex Injection Hybrid Rockets," *Fundamentals of Hybrid Rocket Combustion and Propulsion*, edited by K. Kuo and M. J. Chiaverini, Progress in Astronautics and Aeronautics, chap. Chap. 6, AIAA Progress in Astronautics and Aeronautics, Washington, DC, 2007, pp. 247–276, NSF.

[36]Maicke, B. A., and Majdalani, J., "A Constant Shear Stress Core Flow Model of the Bidirectional Vortex," *Proceedings of the Royal Society of London. Series A*, Vol. 465, No. 2103, 2009, pp. 915–935. doi:10.1098/rspa.2008.0342.

[37]Bejan, A., *Convection Heat Transfer*, John Wiley & Sons, Inc., 3rd ed., 2004.

[38]Morgan, A., "Possible Similarity Solutions of the Laminar, Incompressible, Boundary Layer Equations," *Transactions of the American Society of Mechanical Engineers*, Vol. 80, 1958, pp. 1559.

[39]Morgan, A., "The Reduction by One of the Number of Independent Variables in some Systems of Partial Differential Equations," *The Quarterly Journal of Mathematics*, Vol. 3, No. 1, 1952, pp. 250–259. doi:10.1093/qmath/3.1.250.

[40]Blasius, H., "Grenzschichten in Flüssigkeiten mit Kleiner Reibung," *Zeitschrift für Angewandte Mathematik und Physik (ZAMP)*, Vol. 56, 1908, pp. 1–37.

[41]Saad, T., and Majdalani, J., "Pressure Integration Rules and Restrictions for the Navier-Stokes Equations," *40th Fluid Dynamics Conference and Exhibit*, AIAA Paper 2010-4288, Chicago, Illinois, Aug. 2010.